

# Endogenous $^{17}\text{O}$ DNP of Gd-Doped $\text{CeO}_2$ from 100 to 370 K

Michael A. Hope,<sup>1,2</sup> Snædís Björgvinsdóttir,<sup>1</sup> David M. Halat,<sup>2</sup> Georges Menzildjian,<sup>3</sup> Zhuoran Wang,<sup>3</sup> Bowen Zhang,<sup>4</sup> Judith L. MacManus-Driscoll,<sup>4</sup> Anne Lesage,<sup>3</sup> Moreno Lelli,<sup>5,6</sup> Lyndon Emsley,<sup>1,\*</sup> Clare P. Grey<sup>2,\*</sup>

1. *Institut des Sciences et Ingénierie Chimiques, Ecole Polytechnique Fédérale de Lausanne (EPFL), CH-1015 Lausanne, Switzerland*

2. *Department of Chemistry, University of Cambridge, Lensfield Road, Cambridge, CB2 1EW, UK.*

3. *Centre de RMN à Très Hauts Champs, Université de Lyon (CNRS/ENS de Lyon/UCB-Lyon 1), 69100 Villeurbanne, France.*

4. *Department of Materials Science and Metallurgy, University of Cambridge, Cambridge, CB3 0FS, UK.*

5. *Magnetic Resonance Center (CERM), Department of Chemistry "Ugo Schiff", University of Florence, 50019 Sesto Fiorentino, Italy*

6. *Consorzio Interuniversitario Risonanze Magnetiche MetalloProteine (CIRMMP), via Sacconi 6, 50019 Sesto Fiorentino, Italy*

\* lyndon.emsley@epfl.ch, cpg27@cam.ac.uk

**Keywords:** Solid-state NMR, dynamic nuclear polarization,  $^{17}\text{O}$ ,  $\text{CeO}_2$ , vertically aligned nanocomposite

## Abstract

$^{17}\text{O}$  NMR is an invaluable tool to study the structure and dynamics of oxide materials, but remains challenging to apply in many systems. Even with isotopic enrichment, studies of samples with low masses and/or concentrations of the active species, such as thin films or interfaces, are limited by low sensitivity. Here we show how endogenous dynamic nuclear polarisation (DNP) can dramatically improve sensitivity in the oxide-ion conductor Gd-doped  $\text{CeO}_2$ , with a  $^{17}\text{O}$  enhancement factor of 652 at 100 K. This is the highest enhancement observed so far by endogenous DNP or  $\text{Gd}^{3+}$  DNP, which is explained in terms of the electron paramagnetic resonance characteristics. The DNP properties are studied as a function of Gd concentration for both enriched and natural abundance samples and the buildup behaviour shows that spin diffusion in  $^{17}\text{O}$ -enriched samples improves sensitivity by relaying hyperpolarisation throughout the sample. Notably, efficient hyperpolarisation could still be achieved at elevated temperatures, with enhancement factors of 320 at room temperature and 150 at 370 K, paving the way for characterisation of materials under operational conditions. Finally, the application of endogenous  $\text{Gd}^{3+}$  DNP is illustrated with the study of interfaces in vertically aligned nanocomposite thin films comprised of Gd- $\text{CeO}_2$  nanopillars embedded in a  $\text{SrTiO}_3$  matrix, where DNP affords selective enhancement of the different phases and enables a previously infeasible two-dimensional correlation experiment to be performed showing spin diffusion between Gd- $\text{CeO}_2$  and the solid–solid interface.

## Introduction

A significant proportion of materials of industrial and scientific interest are oxides or contain oxygen;  $^{17}\text{O}$  NMR can therefore provide a wealth of information on the atomic-scale structure and dynamics of these materials.<sup>1</sup> The application of  $^{17}\text{O}$  NMR is hampered, however, by its very low natural abundance (0.037%), which results in low sensitivity.

Dynamic nuclear polarisation (DNP) is a method for enhancing the sensitivity of NMR experiments by harnessing the greater polarisation of unpaired electron spins, via irradiation with microwaves at or near their electron paramagnetic resonance (EPR) frequencies.<sup>2,3</sup> Revolutions in instrumentation and methodology over

the past 20 years have enabled the routine study of solids with DNP at high magnetic field.<sup>2,4</sup> Exogenous DNP, the most common class of DNP experiment today, utilises organic radicals dispersed in a glassy matrix as the source of unpaired electrons to polarize a target substrate.<sup>4</sup> The material is wetted with the radical solution before typically cooling to around 100 K to slow the electron relaxation. In an indirect DNP experiment, the  $^1\text{H}$  hyperpolarisation generated in the vicinity of the organic radicals is relayed by efficient spin diffusion before being transferred to the nucleus of interest by cross polarisation; this affords large bulk enhancements for  $^1\text{H}$  containing solids,<sup>5–7</sup> and strongly surface-selective enhancement of proton-poor materials.<sup>4,8–10</sup> Selective enhancement of the surface region can also be achieved by direct DNP, where the

nucleus of interest is hyperpolarised directly.<sup>10-12</sup>

However, the majority of functional inorganic materials are proton-free and consequently standard DNP techniques cannot be applied to study the internal bulk structure. Two major strategies have been developed to achieve hyperpolarisation of proton-free materials. In relayed DNP, the sample is wetted with an exogenous radical solution and the method relies on spin diffusion of the nucleus of interest to transfer hyperpolarisation from the surface into the bulk.<sup>13-15</sup> In contrast, endogenous DNP utilises paramagnetic electrons present within the material. In metals these are conduction electrons,<sup>16-18</sup> whereas for insulating materials, the radical sources are typically metal ion dopants. This strategy was used extensively for DNP at low fields with static solids,<sup>19-21</sup> but has recently undergone a renaissance with contemporary high-field MAS systems, where endogenous DNP has been demonstrated using high-spin metal ions,<sup>22-27</sup> as well as radical defects generated by gamma irradiation<sup>28</sup> or electrical discharge.<sup>29</sup>

Endogenous DNP has proved highly successful in improving the sensitivity of bulk  $^{17}\text{O}$  NMR of natural abundance oxide materials, with estimated  $^{17}\text{O}$  enhancements in  $\text{Li}_4\text{Ti}_5\text{O}_{12}$  of up to a factor of 282<sup>23,24</sup> (the maximum theoretical enhancement for  $^{17}\text{O}$  is given by the ratio of the electron and nuclear gyromagnetic ratios,  $|\gamma_e/\gamma_n| = 4855$ ). Nevertheless, the standard approach remains to isotopically label the material with  $^{17}\text{O}$ , typically via  $^{17}\text{O}_2$  or  $\text{H}_2^{17}\text{O}$ .<sup>1,30,31</sup> There are, however, systems where even with isotopic enrichment or DNP alone, the applicability of NMR is limited by low sensitivity. For example, surfaces and interfaces are two-dimensional entities which inherently comprise only a small fraction of the sample, so to study them with NMR can be challenging. On the other hand, the structure of such surfaces and interfaces underlies the functionality of many catalytic, electrochemical and electronic processes and applications. Exogenous  $^{17}\text{O}$  DNP NMR has been combined with  $^{17}\text{O}$  enrichment to study the surfaces of  $\text{CeO}_2$ ,<sup>12</sup>  $\text{MgO}$ ,<sup>7</sup>  $\gamma\text{-Al}_2\text{O}_3$ ,<sup>32</sup> and Zr- and Y-based mesoporous silica-supported single-site catalysts,<sup>33</sup> as well as at natural abundance in favourable cases to study  $\text{CeO}_2$  nanorods<sup>34</sup> and surface hydroxyl groups in silica/alumina.<sup>35,36</sup> Exogenous DNP cannot be used to selectively enhance buried solid-solid interfaces, on the other hand, since they lie within the bulk of the material.

Recently we used  $^{17}\text{O}$  NMR to study the interfaces between  $\text{CeO}_2$  nanopillars and a  $\text{SrTiO}_3$  matrix in  $\sim 1\ \mu\text{m}$  thick epitaxially grown thin films.<sup>37</sup> These vertically aligned nanocomposites (VANs) are of significant interest due to their large interfacial areas, enabling the functional properties of thin films, such as their oxidation conductivity, to be enhanced.<sup>38,39</sup> The characterisation of these interfaces represents an important challenge; however, the low sample mass of the thin films, of which only a small proportion corresponds to the interface, results in extremely poor NMR sensitivity even with  $^{17}\text{O}$  enrichment. Our previous experiments were therefore limited to one-dimensional spectra, which still required days of signal averaging in some cases. To improve sensitivity in this and other similarly challenging systems and enable more demanding experiments, in the following we investigate and optimise endogenous DNP in  $^{17}\text{O}$ -enriched  $\text{CeO}_2$  using Gd doping.

$\text{Gd}^{3+}$  can be readily substituted for  $\text{Ce}^{4+}$  in  $\text{CeO}_2$ , with concomitant oxygen vacancies to balance the charge. Gd-doped  $\text{CeO}_2$  is one of the best performing oxide-ion conductors in the intermediate temperature regime (400 – 800 °C) and finds widespread commercial use in solid-oxide fuel cells and oxygen sensors.<sup>40,41</sup> For DNP,  $\text{Gd}^{3+}$  is of interest because its  $f^7$  configuration has no orbital angular momentum ( $L = 0$ ), so that the central transition between the  $m_s = \pm 1/2$  states has a narrow EPR linewidth with a  $g$ -factor close to 2.<sup>3,42,43</sup> Molecular Gd complexes have been developed as alternative polarisation sources for frozen solutions,<sup>42-44</sup> and DNP with endogenous  $\text{Gd}^{3+}$  ions was recently used to power a  $^{17}\text{O}$  radiofrequency maser<sup>26</sup> and probe  $^{89}\text{Y}$ – $^{89}\text{Y}$  correlations in Y-substituted  $\text{CeO}_2$  doped with Gd.<sup>27</sup> Modest enhancements up to a factor of 4 have also been shown by endogenous  $\text{Gd}^{3+}$  DNP in  $\text{Li}_4\text{Ti}_5\text{O}_{12}$ <sup>22</sup> and oxide glasses.<sup>25</sup>

Here we report the EPR and  $^{17}\text{O}$  DNP properties of  $^{17}\text{O}$ -enriched Gd- $\text{CeO}_2$  samples as a function of Gd concentration between 0.01% and 1%, with further comparisons to natural abundance samples. An exceptionally high signal enhancement by a factor of 650 is observed at 100 K for 0.01% Gd- $\text{CeO}_2$ , which remains as high as 150 at 370 K. This establishes the feasibility of endogenous DNP of solids at room temperature and higher, where materials are typically operational, rather than the cryogenic temperatures normally required for efficient DNP. The buildup behaviour shows that the  $^{17}\text{O}$  hyperpolarisation is

relayed by spin diffusion in enriched samples, resulting in significantly faster hyperpolarisation of the sample, and therefore sensitivity, than for natural abundance samples. Finally, the potential of this approach is demonstrated for a sample of vertically aligned nanocomposite Gd-CeO<sub>2</sub>-SrTiO<sub>3</sub> films, for which the different phases and the interfacial environments can be distinguished by their enhancements, and a previously infeasible two-dimensional spectrum could be obtained showing spin diffusion between Gd-CeO<sub>2</sub> and the interface.

## Experimental

Gd-doped CeO<sub>2</sub> was prepared by mixing appropriate ratios of Gd<sub>2</sub>O<sub>3</sub> and CeO<sub>2</sub> to yield Gd concentrations between 0.01 atom% and 1 atom%, with respect to the total metal content (i.e. Gd + Ce). The mixtures were ground by hand, pelletised at 750 MPa under partial vacuum and fired at 1500 °C for two days, before hand-grinding, re-pelletising and firing for a further two days. After hand-grinding again, ~100 mg (~0.6 mmol) was transferred to an alumina tube, placed inside a quartz tube filled with <sup>17</sup>O<sub>2</sub> gas and heated at 1000 °C overnight (70 at% <sup>17</sup>O<sub>2</sub>, NUKEM isotopes, ~20 cm<sup>3</sup>, ~200 mbar at 77 K, ~0.6 mmol). Given the reasonable oxide-ion conductivity of CeO<sub>2</sub> at this temperature, we expect the sample enrichment to be around the maximum of 35 at% for the approximately 1:1 CeO<sub>2</sub>:<sup>17</sup>O<sub>2</sub> molar ratio. For 0.01% and 0.03% Gd-CeO<sub>2</sub>, the initial mixtures were first mixed in a hardened stainless-steel jar using a Retsch PM 100 planetary ball mill, for 2–4 hours at 100–400 rpm. Gd-CeO<sub>2</sub> samples were packed in 3.2 mm outer diameter sapphire rotors.

The Gd-CeO<sub>2</sub>-SrTiO<sub>3</sub> VAN samples were prepared and packed as described previously.<sup>37</sup> Briefly, four 0.5 cm<sup>2</sup> films were deposited on SrTiO<sub>3</sub> substrates with a Sr<sub>3</sub>Al<sub>2</sub>O<sub>6</sub> buffer layer which was then dissolved to lift off the films. The films were center-packed in a 1.3 mm outer-diameter ZrO<sub>2</sub> rotor, with KBr on the top and bottom, before enrichment with <sup>17</sup>O<sub>2</sub> gas at 550 °C overnight.

DNP NMR experiments were performed on a 9.4 T Bruker Avance III spectrometer, with a 263 GHz gyrotron or 265 GHz klystron microwave source, using a low-temperature triple-resonance CPMAS probe for 3.2 mm outer diameter rotors. Where given, the microwave power from the gyrotron was estimated using a calorimeter halfway along the waveguide. The

experiments on Gd-CeO<sub>2</sub>-SrTiO<sub>3</sub> nanopillars were performed with a low-temperature probe for 1.3 mm outer diameter rotors. Spectra were internally referenced to 875 ppm which is the <sup>17</sup>O chemical shift of CeO<sub>2</sub> at ~100 K.<sup>12</sup> The sample temperature was measured by adding a small amount of KBr or Pb(NO<sub>3</sub>)<sub>2</sub> on top of the sample and measuring the temperature dependent <sup>79</sup>Br spin–lattice relaxation constant (*T*<sub>1</sub>)<sup>45</sup> or <sup>207</sup>Pb shift.<sup>46</sup> We note that the <sup>17</sup>O shift of CeO<sub>2</sub> is linear with temperature between 200 – 370 K with a gradient of 0.0168 ± 0.0004 ppm K<sup>-1</sup> and could also be used as an NMR thermometer in this range (Figure S1). Spectra were deconvoluted using the dmfit software.<sup>47</sup> Signal enhancement is defined as the ratio of the peak intensity (*I*) or area (*A*) with and without microwave irradiation, i.e.  $\epsilon_{\text{peak}} = I_{\text{ON}}/I_{\text{OFF}}$ ;  $\epsilon_{\text{area}} = A_{\text{ON}}/A_{\text{OFF}}$ .

EPR spectra were measured using a Bruker EMX nano X-band spectrometer using a 0.4 mT modulation amplitude. Absorption spectra were calculated by integrating the derivative spectra, before background subtraction using the Bruker Xenon software. Spectral simulations were performed using the EasySpin suite in Matlab.<sup>48</sup>

## Results and discussion

Figure 1 shows the <sup>17</sup>O NMR spectrum of <sup>17</sup>O-enriched 0.01% Gd-CeO<sub>2</sub> at 100 K, with and without microwave irradiation, which exhibits a DNP enhancement of 525 ± 5 from the peak intensity or 652 ± 7 from the integrated area. 0.01% Gd corresponds to a concentration of 4.2 mM and an average Gd–Gd distance of 9.1 nm. The enhancement by area is higher because the enhanced signal is broader (Figure 1 inset). There are two reasons for this: (1) the <sup>17</sup>O ions closer to Gd dopants have both a greater enhancement and a broader linewidth due to interaction with the paramagnetic Gd<sup>3+</sup> center,<sup>49</sup> therefore the broader linewidth contributes proportionally more to the overall linewidth of the enhanced signal, and (2) the enhanced magnetization is so large that coupling to the rf-circuit induces radiation damping which acts as an additional source of transverse decay.<sup>50,51</sup> These two factors also cause variation in the linewidth as a function of buildup time (Figure S2): at short buildup times, the signal is dominated by <sup>17</sup>O ions close to Gd<sup>3+</sup> ions which exhibit a broader line; the linewidth decreases with longer buildup time as more distant nuclei are hyperpolarized. However, as the time increases further, the magnetization becomes sufficiently large that radiation

damping becomes comparable to the transverse dephasing time,  $T_2^*$ , and the linewidth increases again. In fact, as we have recently reported, the radiation damping is so strong in 0.01% Gd-CeO<sub>2</sub> and the <sup>17</sup>O signal so sharp that transverse magnetization develops spontaneously when the magnetic field is matched to the negative lobe of the solid effect; the system acts as a radiofrequency maser or raser, resulting in a continuous steady state NMR signal and millihertz linewidths.<sup>26</sup>

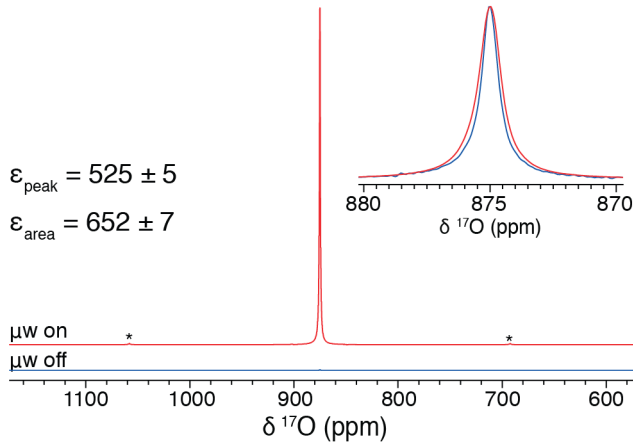


Figure 1: <sup>17</sup>O NMR spectra of <sup>17</sup>O-enriched 0.01% Gd-CeO<sub>2</sub>, with and without ~14 W of microwave ( $\mu$ w) irradiation at 100 K and 10 kHz MAS with a 200 s recycle delay. The magnetic field was optimized for the positive lobe of the solid effect. The enhancements ( $\epsilon$ ) by peak intensity and area are indicated and the inset shows a comparison of the linewidths with normalized intensities.

The large DNP enhancement in Figure 1 predominantly occurs via the solid effect (as shown below), whereby the microwave irradiation drives forbidden transitions which simultaneously flip the electron spin and a nuclear spin.<sup>3</sup> The degree of hyperpolarisation is determined by the EPR properties of the radical, and in particular the linewidth: the narrower the EPR linewidth, the more efficiently microwave irradiation drives the solid effect transitions and the higher the nuclear enhancement, since the excitation width of typical microwave sources is limited. Furthermore, for broad EPR linewidths exceeding the nuclear Larmor frequency, positive and negative enhancement by the solid effect can occur simultaneously and therefore partially cancel out; this is known as the differential solid effect and results in significantly lower enhancement.<sup>3</sup> The EPR linewidth is, therefore, a key factor that determines the enhancement in solid effect DNP and hence we now describe the EPR properties of Gd-CeO<sub>2</sub>.

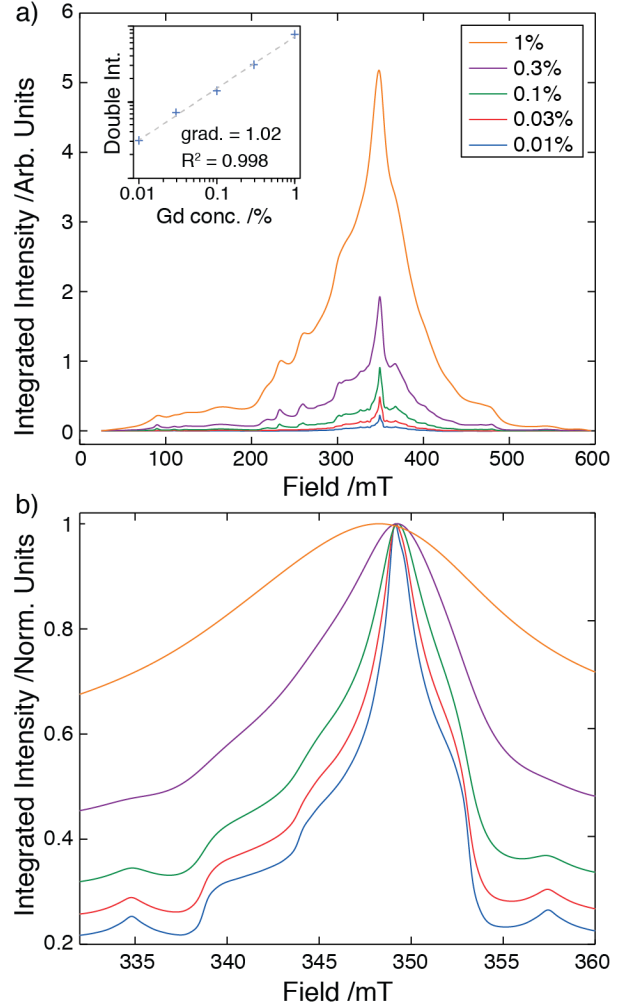


Figure 2: Integrated X-band EPR spectra of Gd-CeO<sub>2</sub> as a function of Gd concentration, with a) absolute scaling and b) normalized intensity. The inset in a) shows a log-log plot of the double integral as a function of nominal concentration.

### EPR Characterization

Figure 2 shows the EPR spectra of Gd-CeO<sub>2</sub> as a function of Gd content between 0.01 atom% and 1 atom%, corresponding to Gd concentrations of 4.2 – 420 mM. With increasing Gd concentration, the resonance is significantly broadened by dipolar coupling, due to the reduction in the average separation of the radicals, from 9.1 nm to 2.0 nm, assuming a random distribution. Aside from dipolar coupling, broadening of EPR spectra of high-spin metal ions is typically caused by 2<sup>nd</sup>-rank zero field splitting (ZFS), which is the interaction of the electron spin with a non-cubic (quadrupolar) charge distribution. At high magnetic field, 2<sup>nd</sup>-rank ZFS can be considered as a perturbation to the Zeeman splitting: the satellite transitions (between  $m_s \neq \pm 1/2$ ) are affected to

first order and significantly broadened, whereas the central transition of a half-integer spin is not affected to first order, resulting in a much sharper resonance which can be used for DNP. The central transition is still broadened at second order, therefore decreasing the ZFS by creating a more isotropic environment around the metal site is an important strategy to improve the DNP enhancement from high-spin metal ions. Indeed, it was recently shown that frozen solutions of Gd(tpatcn), a Gd(III) complex designed to have a more isotropic metal environment and thus a smaller ZFS, exhibited a DNP enhancement a factor of two higher than for frozen solutions of  $[\text{Gd}(\text{dota})(\text{H}_2\text{O})]^-$ .<sup>43</sup>

The metal site in the  $\text{CeO}_2$  lattice, on the other hand, is cubic and the 2<sup>nd</sup>-rank ZFS is zero; this is one of the reasons for the large DNP enhancement in Gd- $\text{CeO}_2$ . However, there is clearly still a significant residual linewidth, even for the lowest Gd concentration, despite the lack of 2<sup>nd</sup>-rank ZFS (Figure 2b). This is due to nonzero coupling to higher order charge distribution multipoles, specifically 4<sup>th</sup>-rank and, to a lesser extent, 6<sup>th</sup>-rank.<sup>52</sup> In a cubic crystal field, these couplings give rise to the following terms in the Hamiltonian:  $B_4(\hat{O}_4^0 + 5\hat{O}_4^4)$  and  $B_6(\hat{O}_6^0 - 21\hat{O}_6^4)$ , where  $\hat{O}_k^q$  are the Stevens operators for crystal field splitting and  $B_4$  and  $B_6$  are the 4<sup>th</sup>- and 6<sup>th</sup>-rank coupling constants, respectively. The EPR spectrum of 0.01% Gd- $\text{CeO}_2$  can be accurately reproduced with  $B_4 = -2.69$  MHz,  $B_6 = -0.89$  kHz, and  $g = 1.99$  (Figure S3);<sup>53,54</sup> for higher concentrations, similar features are observed, but broadened. The higher rank ZFS can be treated perturbatively in an entirely analogous way to 2<sup>nd</sup>-rank ZFS, so while the satellite transitions are broadened to first order, the central transition is only affected at second order, and its linewidth therefore decreases with increasing magnetic field (the width in magnetic field  $\propto B_4^2/\nu_0$ , where  $\nu_0$  is the microwave frequency). Consequently, at 9.4 T, this contribution decreases sufficiently to allow efficient solid effect DNP. Nevertheless, we note that cubic symmetry alone is not sufficient to give a sharp central EPR transition for high-spin metal ions, and thereby efficient DNP; the magnitude of higher order electrostatic multipoles is also important.

Increasing the Gd concentration also introduces more oxygen vacancies which break the cubic symmetry if present close to a Gd ion; this reintroduces the 2<sup>nd</sup>-rank ZFS and would therefore also contribute to the broader EPR spectra. In single crystals of Gd- $\text{CeO}_2$ , the EPR

lines from  $\text{Gd}^{3+}$  in a cubic environment and  $\text{Gd}^{3+}$  in the axial environment arising from an adjacent oxygen vacancy can be clearly resolved; Abraham et al. found that axial signals could only be observed for Gd concentrations of 0.1% or greater, and for 0.02% doping, only the cubic environment was observed, implying weak  $\text{Gd}^{3+}$ -vacancy clustering.<sup>53</sup> This is in good agreement with our experimental observation of zero 2<sup>nd</sup>-rank ZFS in 0.01% Gd- $\text{CeO}_2$ ; nevertheless, broadening from 2<sup>nd</sup>-rank ZFS is expected at higher Gd concentrations.

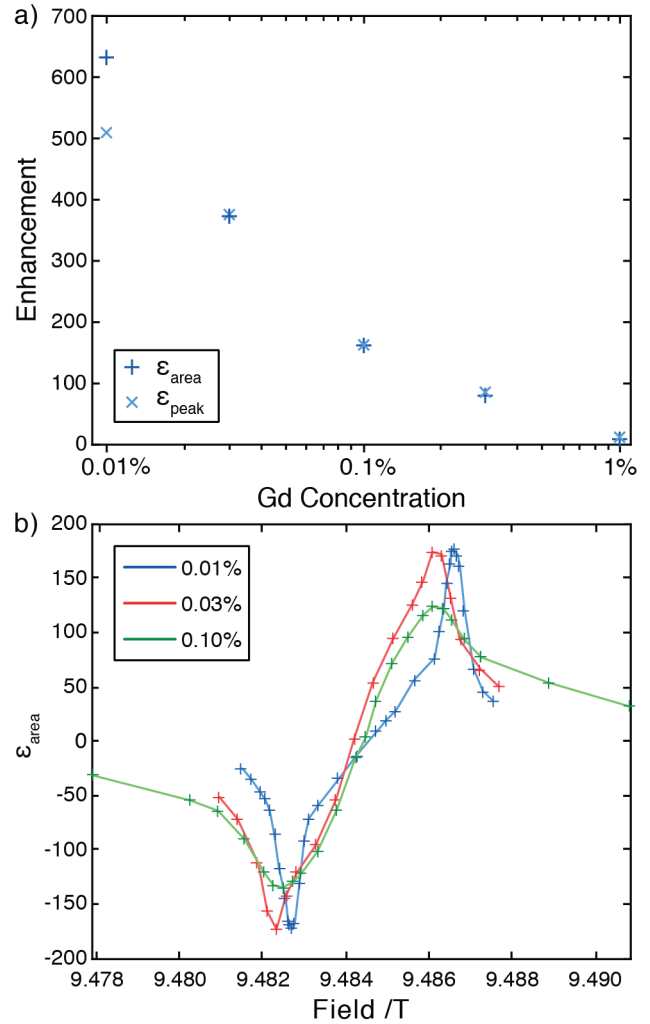


Figure 3: a)  $^{17}\text{O}$  DNP enhancement factors by area as a function of Gd concentration with a 100 s recycle delay and irradiation with a gyrotron source; the solid line is a guide to the eye. b) Field profile showing enhancement by area as a function of magnetic field for different concentrations of Gd, using  $\sim 5$  W of microwave irradiation from a klystron source and a 10 s recycle delay; note that the short recycle delay results in similar enhancements for the different concentrations.

Table 1:  $^{17}\text{O}$  DNP enhancement and buildup characteristics for different Gd-CeO<sub>2</sub> samples. enr. =  $^{17}\text{O}$ -enriched. N.A. = natural abundance.

	0.01%; enr.	0.03%; enr.	0.1%; enr.	0.3%; enr.	0.01%; N.A.	0.1%; N.A.	0.3%; N.A.
$\epsilon_{\text{area}}^{\text{a}}$	652(5)	389(4)	162(3)	81(2)	611(92)	242(37)	112(7)
$T_{\text{B}}/\text{s}^{\text{b}}$	186	109	38.4	7.95	3247	283.5	21.2
$\beta^{\text{b}}$	1.00	1.00	1.00	0.90	0.69	0.74	0.70
$\epsilon_{\text{area}}/\sqrt{T_{\text{B}}}/\text{s}^{-0.5}$	48	37	26	29	11	14	24
$\text{SNR}/\sqrt{t_{\text{exp}}}/\text{s}^{-0.5}$	3009	2414	958	1314	12	22	4.7

<sup>a</sup>The enhancement by area for the recycle delay at which this was largest, i.e. recycle delay  $> T_{\text{B}}$ , see Table S2.

<sup>b</sup>The DNP buildup was fit to  $I = I_0 \left(1 - \exp\left[-\left(\frac{t}{T_{\text{B}}}\right)^{\beta}\right]\right)$ , where  $\beta$  is the stretching exponent, see Figure S7

### Concentration, Sensitivity, and Relay

Due to the increase in EPR linewidth with increasing Gd concentration, the DNP enhancement decreases monotonically (Figure 3a). Decreasing the Gd concentration below 0.01% could potentially increase the DNP enhancement even further; however, at 0.01% the EPR spectrum already appears to be approaching the limiting linewidth as determined by the 4<sup>th</sup>-rank ZFS (Figure 2b) and would not become significantly narrower at lower concentrations. The reduction in number of electron sources could instead then reduce the enhancement. In practice, it is challenging to ensure a uniform distribution of dopants at such low concentrations from solid-state synthesis, and therefore lower concentrations were not attempted here, although this would be interesting to explore in future.

The narrower EPR resonance at low Gd concentration is also reflected in the DNP field profiles (Figure 3b). 0.01% Gd-CeO<sub>2</sub> exhibits sharp positive and negative lobes separated by twice the  $^{17}\text{O}$  Larmor frequency (54.8 MHz, equivalent to 2 mT), corresponding to the resolved solid effect. There is also a broader component of the DNP field profile (see Figure S4) which may correspond to those of the randomly distributed Gd ions that are closer to each other, resulting in a broader central transition resonance from dipolar coupling, or to Gd ions closer to an oxygen vacancy exhibiting greater broadening due to 2<sup>nd</sup>-rank ZFS. The broader profiles seen for 0.03% and 0.1% Gd-CeO<sub>2</sub> more closely resemble those expected for the differential solid effect. There may also be some contribution from the cross effect, for which the positive and negative lobes are spaced by the nuclear Larmor frequency, given that the presence of oxygen vacancies near Gd at higher Gd concentrations will result in heterogeneous broadening

by 2<sup>nd</sup>-rank ZFS; the tensor orientations are determined by the position of the oxygen vacancy, so that the cross effect condition can be achieved between two Gd<sup>3+</sup> ions even within the same crystallite.<sup>3,44</sup> Note that due to time constraints, a 10 s recycle delay was used for the field sweeps which is significantly lower than the buildup time constants ( $T_{\text{B}}$ , see Table 1), resulting in lower enhancements that are similar for all three concentrations. The slight offset between the profiles is ascribed to variations in the microwave frequency of the klystron source, which were not present for the gyrotron source (Figure S5).

The sensitivity in DNP NMR experiments is not determined only by the enhancement, but also by the buildup; the faster hyperpolarization is generated, the more scans can be recorded per unit time.<sup>55,56</sup> The sensitivity gain from DNP can therefore be assessed by considering the parameter  $\epsilon_{\text{area}}/\sqrt{T_{\text{B}}}$ , where  $T_{\text{B}}$  is the DNP buildup time constant. The enhancement and buildup characteristics of different Gd-CeO<sub>2</sub> samples are tabulated in Table 1. Although the buildup becomes slower at lower Gd concentrations, for the  $^{17}\text{O}$ -enriched samples this is less significant than the higher enhancement afforded by more efficient DNP, and the greatest sensitivity is still obtained with the lowest Gd concentration of 0.01%. Paramagnetic quenching, due to strong electron–nuclear coupling in the vicinity of the radical,<sup>56</sup> and depolarization from cross effect-like transitions under MAS in the absence of microwave irradiation<sup>57</sup> can also affect the sensitivity; here, in comparing the sensitivity gains, we neglect the effect of quenching and note that depolarization is not expected to be significant due to minimal cross effect contribution. An alternative analysis, simply measuring the experimental sensitivity as the signal-to-noise ratio

(SNR) per square root of experimental time,<sup>56,58</sup> yields qualitatively similar conclusions (Table 1).

The large DNP enhancement also enables  $^{17}\text{O}$  NMR spectra to be acquired with high sensitivity at natural abundance (Figure S6), as also recently reported in (Y,Gd)- $\text{CeO}_2$ .<sup>27</sup> In this case, on the other hand, the sensitivity is lower for 0.01% Gd- $\text{CeO}_2$  than for 0.1% Gd- $\text{CeO}_2$  due to the extremely slow buildup of the former with  $T_B$  of almost an hour (the experimental sensitivity is then lower for 0.3%, most likely due to significant broadening and quenching). This is because the rate of hyperpolarization falls off with distance from the source as  $1/r^6$ , and at natural abundance (0.037%), the low concentration of  $^{17}\text{O}$  results in weak homonuclear dipolar coupling and inefficient spin diffusion to relay the polarization, so nuclei far from an appropriate source are hyperpolarized only extremely slowly.<sup>59</sup> In contrast, for the enriched samples, magnetization can be relayed away from the sources by spin diffusion and homogenized within the sample, resulting in significantly shorter DNP buildup time constants,  $T_B$ .<sup>60,61</sup> This homogenization is also evidenced by the stretching exponent,  $\beta$ , which is a measure of the distribution of buildup time constants within the sample (Table 1 and Figure S7). For the enriched samples,  $\beta = 1$  indicates a single uniform monoexponential buildup of the sample, whereas for the natural abundance samples  $\beta$  is significantly lower, corresponding to a distribution of buildup time constants and a lack of efficient relay by spin diffusion.<sup>24,60,62</sup> The  $\beta = 0.9$  value for the enriched 0.3% Gd- $\text{CeO}_2$  sample is likely due to the greater relative proportion at higher concentration of  $^{17}\text{O}$  ions that are close enough to  $\text{Gd}^{3+}$  to be polarized directly.

Further evidence for the relay of hyperpolarization can be seen from the dependence of the enhancement on the buildup time (Figure 4).<sup>6,15,60</sup> For  $^{17}\text{O}$ -enriched 0.01% Gd- $\text{CeO}_2$ , the enhancement increases with increasing buildup time up to the order of  $T_B$  (186 s), where it reaches a plateau. This indicates that the relay of hyperpolarization is diffusion limited,<sup>61</sup> as expected for low-gamma  $^{17}\text{O}$ . In contrast, for  $^{17}\text{O}$ -enriched 0.3% Gd- $\text{CeO}_2$ , the enhancement is independent of the buildup time, even below  $T_B$  (8 s) (see also Figure S8). This could be explained by hyperpolarization occurring directly without relay, however in this case the DNP buildup behavior with and without  $^{17}\text{O}$  enrichment would be the same, whereas the buildup of  $^{17}\text{O}$ -enriched 0.3% Gd- $\text{CeO}_2$  is still notably faster than at natural

abundance (Table 1), with, as previously noted, a stretching factor  $\beta = 0.9$  compared to  $\beta = 0.7$  at natural abundance; both of these observations indicate that hyperpolarization still occurs by relay with 0.3% Gd doping. Instead, the flat enhancement vs. buildup time in this sample is ascribed to a transition from the spin-diffusion limited regime to the “spin-exchange” regime,<sup>61</sup> where the rate-limiting step becomes the transfer of polarization away from nuclei in the immediate vicinity of the radical, i.e., across the spin-diffusion barrier. This transition is expected with increasing Gd concentration because the average Gd–Gd distance decreases, decreasing the distance over which hyperpolarization must diffuse, so that this is no longer rate limiting. We note that based on the Gd concentration dependence of the  $^{17}\text{O}$   $T_1$ , direct hyperpolarization would be expected at concentrations above 0.3% even in enriched samples; see Figure S9 and discussion in the SI. For natural abundance 0.01% Gd- $\text{CeO}_2$ , there is some evidence of relay at the longest buildup times since the observed enhancement increases (Figure 4); however, due to the low sensitivity without DNP, the errors are too great to say for certain. As the zero-quantum  $^{17}\text{O}$  lineshape is not dominated by homonuclear dipolar coupling, the spin diffusivity,  $D$ , depends on the nuclear spin concentration as  $D \propto (c_{\text{nuc}})^{4/3}$  (see Supplementary Note 1);<sup>63</sup> therefore, the spin diffusivity at natural abundance is almost four orders of magnitude lower than at 35% enrichment. Nevertheless, given the long  $T_1$ , some relay may still be possible.

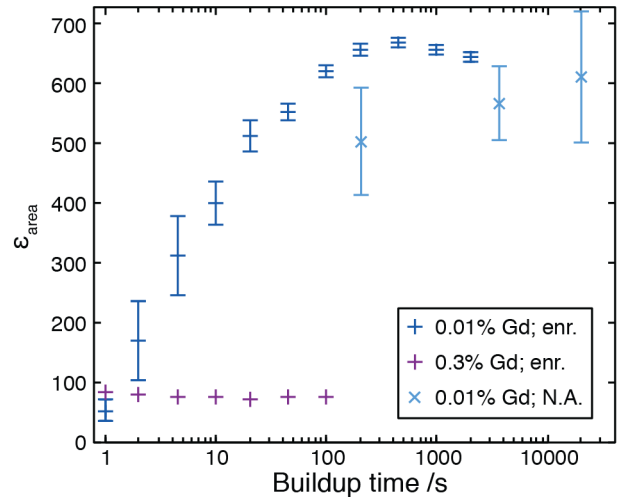


Figure 4:  $^{17}\text{O}$  enhancement by area as a function of buildup time for  $^{17}\text{O}$  enriched (enr.) 0.01% and 0.3% Gd- $\text{CeO}_2$  and natural abundance (N.A.) 0.01% Gd- $\text{CeO}_2$ . For 0.3% Gd the error bars are smaller than the markers.



The enhancement of 652 for 0.01% Gd-CeO<sub>2</sub> is the highest that has been reported for DNP with a high-spin metal ion. In part this arises from the relatively low gyromagnetic ratio of <sup>17</sup>O, since the maximum possible DNP enhancement is given by  $|\gamma_e/\gamma_n|$ , the ratio of the electron and nuclear gyromagnetic ratios ( $|\gamma_e/\gamma_n| = 4855$  for <sup>17</sup>O). However, even scaling by the nuclear gyromagnetic ratio, the <sup>17</sup>O enhancement in Gd-CeO<sub>2</sub> is more than a factor of two higher than the best performing organic Gd<sup>3+</sup> complex, Gd(tpatcn),<sup>43</sup> for direct <sup>1</sup>H, <sup>13</sup>C, and <sup>15</sup>N experiments (Table 2). This is not due to a narrower EPR resonance because although Gd-CeO<sub>2</sub> is cubic and has no 2<sup>nd</sup>-rank ZFS, the 4<sup>th</sup>-rank coupling actually results in a broader EPR resonance than in Gd(tpatcn): the 2<sup>nd</sup> order broadening of the central transition for  $B_4 = -2.69$  MHz yields a linewidth comparable to that from a 2<sup>nd</sup>-rank ZFS of  $D = 500 - 600$  MHz, whereas for Gd(tpatcn)  $D \approx 410$  MHz.<sup>43</sup> Instead, the greater enhancement is ascribed to the long <sup>17</sup>O  $T_1$ , which allows greater nuclear magnetization to accumulate. Stronger Gd-<sup>17</sup>O hyperfine coupling in Gd-CeO<sub>2</sub> could also play a role: the first oxygen shell is found at a distance of 2.34 Å, compared to nearest Gd-H distances of  $\sim 3.7$  Å in Gd complexes;<sup>64</sup> this results in stronger dipolar coupling, which increases the probability of the nominally forbidden solid effect transitions. Delocalization of the unpaired electron density could also contribute to the anisotropic hyperfine coupling, and hence the solid effect. Hyperpolarization may also be mediated by the second coordination shell (at 4.49 Å) with smaller hyperfine coupling. The lower enhancement observed for <sup>89</sup>Y in (Y,Gd)-CeO<sub>2</sub><sup>27</sup> could be due to the relatively high concentration of Y dopants (10–40%), and concomitant oxygen vacancies, which break the cubic symmetry of the metal site, introducing 2<sup>nd</sup>-rank ZFS and broadening of the EPR resonance. The much lower enhancement of previous endogenous Gd<sup>3+</sup> DNP experiments,  $\epsilon < 4$ ,<sup>22,25</sup> is ascribed to the broad EPR resonances caused by ZFS or dipolar coupling. The higher enhancement of 0.01% Gd-CeO<sub>2</sub> than endogenous DNP<sup>23,24</sup> of natural abundance Mn<sup>2+</sup>- or Fe<sup>3+</sup>-doped Li<sub>4</sub>Ti<sub>5</sub>O<sub>12</sub> is ascribed to the narrow EPR resonance and long <sup>17</sup>O  $T_1$  in Gd-CeO<sub>2</sub>. In cases where the <sup>17</sup>O  $T_1$  is shorter, <sup>17</sup>O enrichment is also advantageous since it allows hyperpolarization to be more quickly relayed throughout the sample by spin diffusion.

Table 2: The highest observed direct enhancements from Gd<sup>3+</sup> DNP at  $\sim 100$  K,  $|\epsilon_{\text{top}}|$ , the maximum theoretical enhancement,  $|\epsilon_{\text{theor}}|$ , as determined by the ratio of the nuclear and electron gyromagnetic ratios ( $\epsilon_{\text{theor}} = \gamma_e/\gamma_n$ ), and the relative enhancement.

Nucleus	$ \gamma_n $ /MHz T <sup>-1</sup>	$ \epsilon_{\text{top}} $	$ \epsilon_{\text{theor}} $	$\frac{\epsilon_{\text{top}}}{\epsilon_{\text{theor}}}$
<sup>17</sup> O	5.772	652 <sup>a</sup>	4855	13.4%
<sup>1</sup> H	42.577	37 <sup>b</sup>	658	5.6%
<sup>13</sup> C	10.708	122 <sup>b</sup>	2617	4.7%
<sup>15</sup> N	4.316	350 <sup>b</sup>	6493	5.4%
<sup>89</sup> Y	2.095	193 <sup>c</sup>	13377	1.4%

<sup>a</sup>0.01% Gd-CeO<sub>2</sub>, this study

<sup>b</sup>Gd(tpatcn), Stevanato et al.<sup>43</sup>

<sup>c</sup>(Y,Gd)-CeO<sub>2</sub>, Jardón-Álvarez et al.<sup>27</sup>

### High temperature DNP

A key limitation of current exogenous MAS DNP approaches is the requirement for low temperatures. Typically, the radical/solvent combinations in use today only provide efficient DNP (e.g.  $\epsilon_H > 100$ ) at temperatures around  $\sim 100$  K. Some of the earliest MAS DNP measurements were performed at room temperature, with a BDPA/polystyrene formulation, but the enhancements were relatively low ( $\epsilon_H \approx 10$ ).<sup>65</sup> More efficient DNP at room temperature has been reported using *ortho*-terphenyl as the matrix ( $\epsilon_H \approx 15 - 20$ ),<sup>66</sup> but it is only metastable at room temperature, with a glass transition temperature of 243 K, and melts at 330 K.

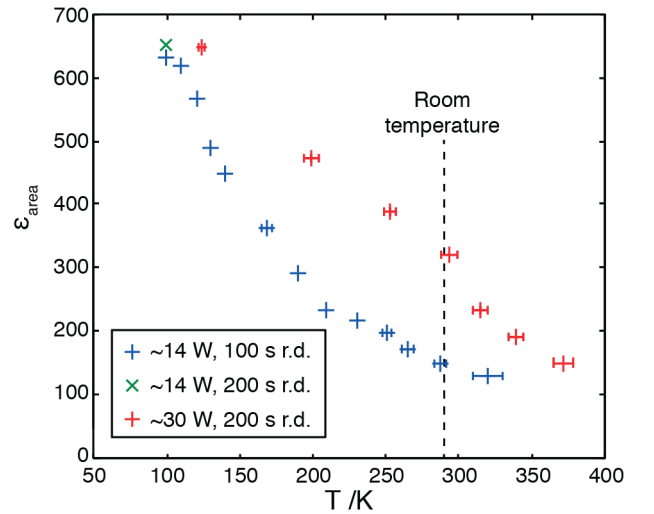


Figure 5: <sup>17</sup>O enhancement by area as a function of temperature for <sup>17</sup>O enriched 0.01% Gd-CeO<sub>2</sub> (see Figure S10 for peak enhancement). Data is shown with microwave powers of  $\sim 14$  W and  $\sim 30$  W and recycle delays (r.d.) of 100 s and 200 s, respectively. For



the ~14 W dataset, the temperature was measured using KBr and the error bars represent uncertainty in the sample temperature. For the ~30 W dataset the temperature was measured using Pb(NO<sub>3</sub>)<sub>2</sub>, since KBr is not accurate at high temperatures, and the error bars indicate the distribution of temperature within the sample. The enhancements were calculated by recording spectra with and without microwave irradiation at the same sample temperature, except for the points recorded with ~30 W above room temperature, for which the enhancements were all measured relative to the microwave off spectrum at 293 K; these enhancements are therefore slightly underestimated.

In Gd-CeO<sub>2</sub>, on the other hand, the metal dopants are dispersed within a rigid crystalline lattice with a melting point of 2400 °C. As a result, the DNP performance can be assessed at temperatures above the glass transition temperature of typical DNP matrices. We note that room temperature <sup>29</sup>Si DNP was also recently demonstrated in quartz using endogenous radical defects from irradiation with gamma rays.<sup>28</sup> Here we measure the DNP enhancements for 0.01% Gd-CeO<sub>2</sub> up to 370 K (Figure 5). Two sets of experiments were performed, one using a microwave power of ~14 W (as in Figure 1) and a recycle delay of 100 s, the other using a higher microwave power of ~30 W and a recycle delay of 200 s. In both cases, the enhancement decreases with increasing temperature; this is ascribed to more efficient electron relaxation, which reduces the saturation of the EPR resonance and reduces the DNP efficiency. This reduces the saturation of the solid effect transition and increases the rate at which nuclear polarization is lost, but also results in the reduction in  $T_B$  with temperature (Figure S11). The sensitivity decreases overall with temperature because it is determined by the DNP enhancement, the Boltzmann population, and the build-up time constant: sensitivity  $\propto \frac{\epsilon_{\text{area}}}{T\sqrt{T_{\text{DNP}}}}$  (Table S1 and Figure S12); nevertheless, at any given experimental temperature, DNP increases sensitivity by more than two orders of magnitude. In particular, at room temperature (~290 K), large <sup>17</sup>O enhancement factors of 149 at ~14 W and 321 at ~30 W are still observed. The higher microwave power results in more effective saturation of the solid effect transition, and hence a greater enhancement across the temperature range. However, the higher power also results in greater sample heating so that the lowest possible temperature was 124 K with ~30 W, compared to 100 K for ~14 W. In this case, the higher temperature counteracts the higher power, resulting in a maximum enhancement factor of 648 with ~30 W, very similar to the 652 achieved at 100 K with ~14 W (the maximum enhancement observed with a recycle delay of 100 s is

slightly lower at 632). Significant DNP enhancements were also observed above room temperature, with an enhancement factor of 150 at 370 K with ~30 W of microwave power, the highest temperature at which solid effect DNP has been reported, to our knowledge. Here the temperature was limited only by the probe which is designed to operate at cryogenic temperatures. At these temperatures, the vacancy mobility in Gd-CeO<sub>2</sub> may approach the <sup>17</sup>O spin diffusivity, based on extrapolation from high temperature conductivity measurements.<sup>67</sup> However, this is unlikely to contribute to significant long-range relay of hyperpolarization since the ionic conduction is vacancy mediated: although the vacancy may hop between multiple sites, each oxygen ion will only hop once (from its original site, to the vacant site nearby). Nevertheless, physical exchange could still play a role in increasing the flow of hyperpolarization the short distance across the spin diffusion barrier, where electron–nuclear coupling significantly reduces spin diffusion, especially given that vacancies are more likely to be present in the vicinity of the Gd dopants for electrostatic reasons.<sup>67,68</sup>

There are many systems that are important to study under operational conditions at or above room temperature, to probe, for example, dynamics (including oxide-ion mobility), phase transitions and other in-situ behavior more generally. Extending the applicability of solid-state DNP to these temperatures should allow greatly improved sensitivity to perform more demanding NMR experiments on challenging systems.

### *Gd-CeO<sub>2</sub>-SrTiO<sub>3</sub> VAN Films*

To demonstrate the utility of DNP in systems which are a challenge for conventional NMR, even with <sup>17</sup>O enrichment, a vertically aligned nanocomposite of 1% Gd-CeO<sub>2</sub>-SrTiO<sub>3</sub> was studied. This concentration was chosen because high concentrations of Gd are typically used to enhance ionic conductivity in CeO<sub>2</sub>. By simultaneously depositing Gd-CeO<sub>2</sub> and SrTiO<sub>3</sub> as an epitaxial thin film, nanopillars of Gd-CeO<sub>2</sub> can be grown with ~20 nm diameter.<sup>69,70</sup> To prevent dilution of the sample, the substrate was removed using a lift-off procedure<sup>37</sup> giving a sample mass of ~0.5 mg, before packing in a 1.3 mm outer-diameter ZrO<sub>2</sub> rotor, then enriching with <sup>17</sup>O<sub>2</sub> gas.

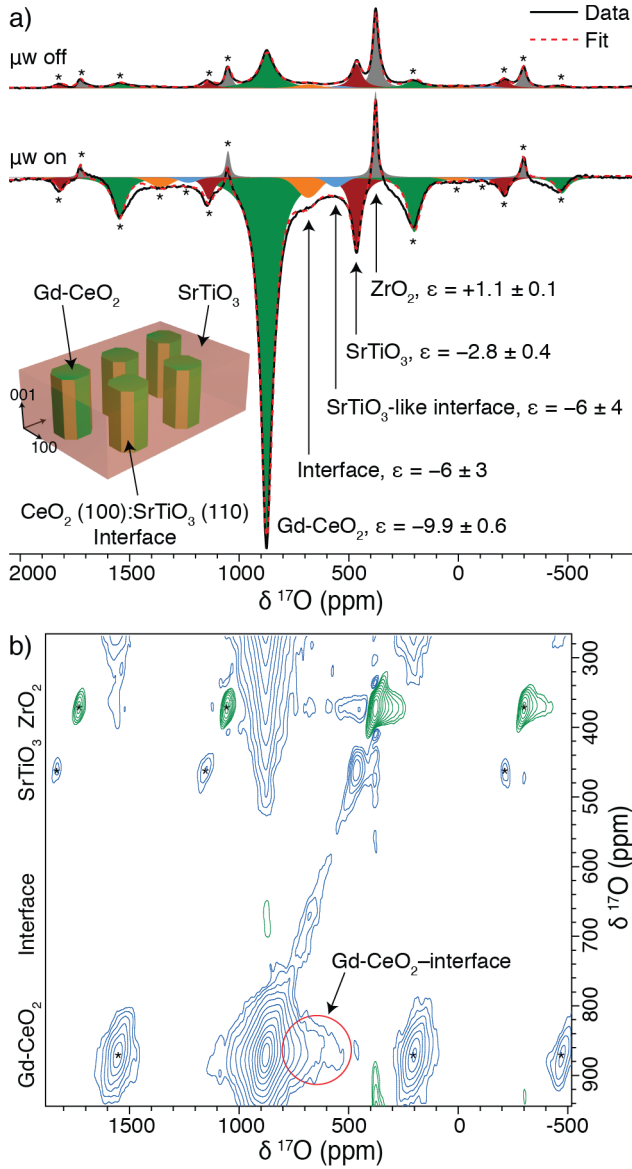


Figure 6: a)  $^{17}\text{O}$  NMR spectra of 1% Gd-doped  $\text{CeO}_2$ - $\text{SrTiO}_3$  VAN films, with and without  $\sim 40$  W of microwave irradiation, with the deconvolution and corresponding peak enhancements,  $\epsilon$ . The assignments are as determined in Reference <sup>37</sup>. A schematic of the nanopillars is inset, with the  $\text{SrTiO}_3$  crystal axes shown. b) DNP-enhanced  $^{17}\text{O}$  EXSY spectrum, showing a cross peak between the Gd- $\text{CeO}_2$  and interface signals, recorded with a 0.1 s mixing time and 38 increments of  $27 \mu\text{s}$  in the indirect dimension. Spectra were recorded at 37 kHz MAS in a 1.3 mm MAS DNP probe with a sample temperature of 140 K and recycle delays of a) 1 s and b) 4.2 s. Blue and green contours indicate positive and negative intensity, respectively, and asterisks indicate spinning sidebands. We note that the sample is placed in the center of the  $\text{ZrO}_2$  rotor, and thus will experience a more uniform  $B_1$  field than the rotor itself, likely contributing to the slight mis-phasing of the  $\text{ZrO}_2$  signal.

Figure 6a shows the  $^{17}\text{O}$  NMR spectra of the VAN films at 140 K, with and without microwave irradiation. The magnetic field was optimized for the negative lobe of the solid effect to allow unenhanced background signals to be readily distinguished by their opposite phase. The Gd- $\text{CeO}_2$  signal at 875 ppm is enhanced by  $\epsilon_{\text{peak}} = -9.9$ , in line with the results on bulk 1% Gd- $\text{CeO}_2$  ( $\epsilon = 8.5$ ); although the Gd concentration is much higher than would be ideal for DNP, this nevertheless demonstrates the applicability of the technique. The  $\text{SrTiO}_3$  signal at 465 ppm has a significantly lower enhancement of  $\epsilon_{\text{peak}} = -2.8$  because the  $\text{Gd}^{3+}$  is predominantly present in the Gd- $\text{CeO}_2$  phase, and enhancement of the  $\text{SrTiO}_3$  can only therefore occur by longer distance  $\text{Gd}^{3+}$ - $^{17}\text{O}$  interactions or minor substitution of Gd into the  $\text{SrTiO}_3$  phase (we note that significant relay of hyperpolarization from Gd- $\text{CeO}_2$  to  $\text{SrTiO}_3$  on this timescale can be ruled out by the lack of a cross peak in the EXSY spectrum, see below). In contrast, the  $\text{ZrO}_2$  signal at 377 ppm from the partially  $^{17}\text{O}$ -enriched rotor, which is not in atomic scale contact with  $\text{Gd}^{3+}$ , is not enhanced and remains positive.

Between the Gd- $\text{CeO}_2$  and  $\text{SrTiO}_3$  peaks, two signals can be distinguished, which have been assigned previously on the basis of random structure searching and density functional theory calculations.<sup>37</sup> The major signal at 685 ppm arises from the  $\text{CeO}_2$  (100): $\text{SrTiO}_3$  (110) interface (yellow in Figure 6a inset); this facet comprises a shared oxide layer between the  $\text{CeO}_2$  and  $\text{SrTiO}_3$  phases and has a chemical shift intermediate between the two. The intensity around 465 ppm is caused by  $\text{SrTiO}_3$ -like environments in the major  $\text{CeO}_2$  (110): $\text{SrTiO}_3$  (100) interface (green in Figure 6a inset). Both interface signals exhibit an enhancement of  $\epsilon \approx -6$ , i.e. intermediate between those of Gd- $\text{CeO}_2$  and  $\text{SrTiO}_3$ . This is consistent with environments that are adjacent to the Gd- $\text{CeO}_2$  phase, although there is a significant uncertainty in the values of  $\epsilon$  due to the weakness of the signals.

The use of a DNP system with 1.3 mm diameter rotors, rather than the standard 3.2 mm rotors, was critical here for two reasons. Firstly, this allows a smaller NMR coil to be used which, given the extremely low sample mass, increases the fill factor and hence the signal-to-noise ratio. Secondly, the smaller rotors enable faster MAS to separate the spinning sidebands from the wide isotropic chemical shift range spanning over 500 ppm, which is only just achieved at 37 kHz MAS. Overlapping

spinning sidebands would obscure the weak interface signals in the already cluttered spectrum.

The enhancement afforded by DNP enabled the 1D spectrum to be acquired in two hours, compared to a day to acquire the spectrum at room temperature without DNP, and five days for the same mass of sample without Gd doping. Significantly, it allows previously infeasible 2D experiments: Figure 6b shows a DNP-enhanced  $^{17}\text{O}$  exchange spectroscopy (EXSY) spectrum acquired in 36 hours. The Gd-CeO<sub>2</sub>, SrTiO<sub>3</sub>, and interface signals are again inverted, and the interface signal is more clearly resolved. More importantly, although the intensity is weak, a cross peak appears to be present between the Gd-CeO<sub>2</sub> and interface signals, corresponding to transfer of hyperpolarization generated in the Gd-CeO<sub>2</sub> phase to the interface (see also Figure S13); note that physical exchange of oxide-ions is extremely slow at 140 K. The absence of the other symmetric cross peak (from the interface to Gd-CeO<sub>2</sub>) indicates that the hyperpolarization is predominantly generated in the Gd-CeO<sub>2</sub> phase.<sup>71</sup> The signal of the cross peak is comparatively weak and transfer over a greater distance to SrTiO<sub>3</sub> cannot be seen because  $^{17}\text{O}$  spin diffusion is slow and the diffusion time is limited by the short  $T_1$  induced by the high Gd<sup>3+</sup> concentration. This spectrum demonstrates the feasibility of performing 2D  $^{17}\text{O}$  experiments and observing correlations in sub-milligram samples by combining  $^{17}\text{O}$  enrichment with endogenous DNP. More distant correlations could potentially be observed with lower Gd<sup>3+</sup> concentrations in this and similar systems due to the resulting longer  $T_1$  and greater enhancement.

## Conclusions

An enhancement of 650 has been observed for the  $^{17}\text{O}$  signal in 0.01% Gd-CeO<sub>2</sub> from endogenous DNP, which represents the highest reported enhancement for endogenous DNP or Gd<sup>3+</sup> DNP, even when correcting for the gyromagnetic ratio. This is ascribed to the narrow EPR resonance arising from the cubic metal site in CeO<sub>2</sub>, although 4<sup>th</sup>-rank coupling is significant, as well as the long  $^{17}\text{O}$   $T_1$  constant. The enhancement decreases with increasing Gd concentration due to dipolar broadening of the EPR resonance.

The DNP buildup behaviour shows that  $^{17}\text{O}$  hyperpolarisation is relayed by spin diffusion in enriched samples, resulting in significantly faster buildup, and therefore sensitivity, than for natural

abundance samples, although natural abundance spectra can still be recorded quickly using DNP. The enhancement decreases with increasing temperature, but since the crystalline DNP matrix is rigid and does not melt, DNP remained effective, with  $^{17}\text{O}$  enhancement factors of 320 at room temperature and 150 at the highest studied temperature of 370 K. This shows great promise for characterisation of structure and dynamics under more relevant conditions for e.g., catalysis or studies of solid-state electrolytes.

Finally, endogenous Gd<sup>3+</sup> DNP was applied to a vertically aligned nanocomposite thin film sample of Gd-CeO<sub>2</sub>-SrTiO<sub>3</sub> with a very low sample mass of ~0.5 mg and partial  $^{17}\text{O}$ -enrichment. The different phases could be distinguished by their enhancements, with the highest for Gd-CeO<sub>2</sub>, the lowest for SrTiO<sub>3</sub>, and intermediate enhancements for the interface signals. The enhanced sensitivity enabled a previously infeasible 2D EXSY spectrum to be recorded which shows transfer of polarisation from the Gd-CeO<sub>2</sub> nanopillars to the interface, corroborating the assignment of the interface signal. Together this work shows how endogenous DNP can be combined with  $^{17}\text{O}$  enrichment to perform advanced characterisation experiments on extremely challenging samples.

## Supplementary Information

Supplementary information contains additional NMR, DNP and EPR figures.

Raw and processed NMR and EPR data are freely available at DOI: [10.5281/zenodo.5101215](https://doi.org/10.5281/zenodo.5101215).

## Acknowledgements

This work was supported by Swiss National Science Foundation Grant No. 200020\_178860. J.L.M.-D. acknowledges support from the Royal Academy of Engineering Grant, CIET1819\_24. A.L. gratefully acknowledges financial support from the ANR contract 17-CE29-0006-01. M.L. gratefully acknowledges Fondazione CR Firenze. We would like to thank Gabriele Stevanato for useful discussions.

## References

1. Ashbrook, S. E.; Smith, M. E., Solid state  $^{17}\text{O}$  NMR—an introduction to the background principles and applications to inorganic materials. *Chem. Soc. Rev.* **2006**, 35 (8), 718–35.
2. Ni, Q. Z.; Daviso, E.; Can, T. V.; Markhasin, E.; Jawa, S. K.; Swager, T. M.; Temkin, R. J.; Herzfeld, J.; Griffin, R.

- G., High Frequency Dynamic Nuclear Polarization. *Acc. Chem. Res.* **2013**, *46* (9), 1933–1941.
3. Lilly Thankamony, A. S.; Wittmann, J. J.; Kaushik, M.; Corzilius, B., Dynamic nuclear polarization for sensitivity enhancement in modern solid-state NMR. *Prog. Nucl. Magn. Reson. Spectrosc.* **2017**, *102–103*, 120–195.
4. Rossini, A. J.; Zagdoun, A.; Lelli, M.; Lesage, A.; Copéret, C.; Emsley, L., Dynamic Nuclear Polarization Surface Enhanced NMR Spectroscopy. *Acc. Chem. Res.* **2013**, *46* (9), 1942–1951.
5. van der Wel, P. C. A.; Hu, K.-N.; Lewandowski, J.; Griffin, R. G., Dynamic Nuclear Polarization of Amyloidogenic Peptide Nanocrystals: GNNQQNY, a Core Segment of the Yeast Prion Protein Sup35p. *J. Am. Chem. Soc.* **2006**, *128* (33), 10840–10846.
6. Rossini, A. J.; Zagdoun, A.; Hegner, F.; Schwarzwald, M.; Gajan, D.; Coperet, C.; Lesage, A.; Emsley, L., Dynamic nuclear polarization NMR spectroscopy of microcrystalline solids. *J. Am. Chem. Soc.* **2012**, *134* (40), 16899–16908.
7. Blanc, F.; Sperrin, L.; Jefferson, D. A.; Pawsey, S.; Rosay, M.; Grey, C. P., Dynamic nuclear polarization enhanced natural abundance  $^{17}\text{O}$  spectroscopy. *J. Am. Chem. Soc.* **2013**, *135* (8), 2975–2978.
8. Lesage, A.; Lelli, M.; Gajan, D.; Caporini, M. A.; Vitzthum, V.; Miéville, P.; Alauzun, J.; Roussey, A.; Thieuleux, C.; Mehdi, A., et al., Surface Enhanced NMR Spectroscopy by Dynamic Nuclear Polarization. *J. Am. Chem. Soc.* **2010**, *132* (44), 15459–15461.
9. Lelli, M.; Gajan, D.; Lesage, A.; Caporini, M. A.; Vitzthum, V.; Mieville, P.; Heroguel, F.; Rascon, F.; Roussey, A.; Thieuleux, C., et al., Fast characterization of functionalized silica materials by silicon-29 surface-enhanced NMR spectroscopy using dynamic nuclear polarization. *J. Am. Chem. Soc.* **2011**, *133* (7), 2104–2107.
10. Lee, D.; Duong, N. T.; Lafon, O.; De Paëpe, G., Primostrato Solid-State NMR Enhanced by Dynamic Nuclear Polarization: Pentacoordinated  $\text{Al}^{3+}$  Ions Are Only Located at the Surface of Hydrated  $\gamma$ -Alumina. *J. Phys. Chem. C* **2014**, *118* (43), 25065–25076.
11. Lafon, O.; Rosay, M.; Aussenac, F.; Lu, X.; Trebosc, J.; Cristini, O.; Kinowski, C.; Touati, N.; Vezin, H.; Amoureux, J. P., Beyond the silica surface by direct silicon-29 dynamic nuclear polarization. *Angew. Chem. Int. Ed. Engl.* **2011**, *50* (36), 8367–8370.
12. Hope, M. A.; Halat, D. M.; Magusin, P. C.; Paul, S.; Peng, L.; Grey, C. P., Surface-Selective Direct  $^{17}\text{O}$  DNP NMR of  $\text{CeO}_2$  Nanoparticles. *Chem. Commun.* **2017**, *53* (13), 2142–2145.
13. Björgvinsdóttir, S.; Walder, B. J.; Pinon, A. C.; Emsley, L., Bulk Nuclear Hyperpolarization of Inorganic Solids by Relay from the Surface. *J. Am. Chem. Soc.* **2018**, *140* (25), 7946–7951.
14. Björgvinsdóttir, S.; Walder, B. J.; Matthey, N.; Emsley, L., Maximizing Nuclear Hyperpolarization in Pulse Cooling under MAS. *J. Magn. Reson.* **2019**, *300*, 142–148.
15. Björgvinsdóttir, S.; Moutzouri, P.; Berruyer, P.; Hope, M. A.; Emsley, L., Sensitivity Enhancements in Lithium Titanates by Incipient Wetness Impregnation DNP NMR. *J. Phys. Chem. C* **2020**, *124* (30), 16524–16528.
16. Overhauser, A. W., Polarization of Nuclei in Metals. *Phys. Rev.* **1953**, *92* (2), 411–415.
17. Carver, T. R.; Slichter, C. P., Polarization of Nuclear Spins in Metals. *Phys. Rev.* **1953**, *92* (1), 212–213.
18. Hope, M. A.; Rinkel, B. L. D.; Gunnarsdóttir, A. B.; Märker, K.; Menkin, S.; Paul, S.; Sergeyev, I. V.; Grey, C. P., Selective NMR observation of the SEI–metal interface by dynamic nuclear polarisation from lithium metal. *Nat. Commun.* **2020**, *11* (1), 2224.
19. Schmugge, T. J.; Jeffries, C. D., High Dynamic Polarization of Protons. *Phys. Rev.* **1965**, *138* (6A), A1785–A1801.
20. Brun, E.; Derighetti, B.; Hundt, E. E.; Niebuhr, H. H., NMR of  $^{17}\text{O}$  in ruby with dynamic polarization techniques. *Phys. Lett. A* **1970**, *31* (8), 416–417.
21. Atsarkin, V. A., Dynamic polarization of nuclei in solid dielectrics. *Sov. Phys. Uspekhi* **1978**, *21* (9), 725–745.
22. Chakrabarty, T.; Goldin, N.; Feintuch, A.; Houben, L.; Leskes, M., Paramagnetic Metal-Ion Dopants as Polarization Agents for Dynamic Nuclear Polarization NMR Spectroscopy in Inorganic Solids. *ChemPhysChem* **2018**, *19* (17), 2139–2142.
23. Wolf, T.; Kumar, S.; Singh, H.; Chakrabarty, T.; Aussenac, F.; Frenkel, A. I.; Major, D. T.; Leskes, M., Endogenous Dynamic Nuclear Polarization for Natural Abundance  $^{17}\text{O}$  and Lithium NMR in the Bulk of Inorganic Solids. *J. Am. Chem. Soc.* **2019**, *141* (1), 451–462.
24. Jardon-Alvarez, D.; Reuveni, G.; Harchol, A.; Leskes, M., Enabling Natural Abundance  $^{17}\text{O}$  Solid-State NMR by Direct Polarization from Paramagnetic Metal Ions. *J. Phys. Chem. Lett.* **2020**, *11* (14), 5439–5445.
25. Paterson, A. L.; Perras, F. A.; Besser, M. F.; Pruski, M., Dynamic Nuclear Polarization of Metal-Doped Oxide Glasses: A Test of the Generality of Paramagnetic Metal Polarizing Agents. *J. Phys. Chem. C* **2020**, *124* (42), 23126–23133.
26. Hope, M. A.; Björgvinsdóttir, S.; Grey, C. P.; Emsley, L., A Magic Angle Spinning Activated  $^{17}\text{O}$  DNP Raser. *J. Phys. Chem. Lett.* **2021**, *12*, 345–349.
27. Jardon-Alvarez, D.; Kahn, N.; Houben, L.; Leskes, M., Oxygen Vacancy Distribution in Yttrium-Doped Ceria from  $^{89}\text{Y}$ – $^{89}\text{Y}$  Correlations via Dynamic Nuclear Polarization Solid-State NMR. *J. Phys. Chem. Lett.* **2021**, *12* (11), 2964–2969.
28. Carnahan, S. L.; Venkatesh, A.; Perras, F. A.; Wishart, J. F.; Rossini, A. J., High-Field Magic Angle Spinning Dynamic Nuclear Polarization Using Radicals Created by  $\gamma$ -Irradiation. *J. Phys. Chem. Lett.* **2019**, *10* (17), 4770–4776.
29. Katz, I.; Blank, A., Dynamic nuclear polarization in solid samples by electrical-discharge-induced radicals. *J. Magn. Reson.* **2015**, *261*, 95–100.

30. Gerothanassis, I. P., Oxygen-17 NMR spectroscopy: basic principles and applications (part I). *Prog. Nucl. Magn. Reson. Spectrosc.* **2010**, *56* (2), 95–197.
31. Metro, T. X.; Gervais, C.; Martinez, A.; Bonhomme, C.; Laurencin, D., Unleashing the Potential of  $^{17}\text{O}$  NMR Spectroscopy Using Mechanochemistry. *Angew. Chem. Int. Ed. Engl.* **2017**, *56* (24), 6803–6807.
32. Li, W.; Wang, Q.; Xu, J.; Aussenac, F.; Qi, G.; Zhao, X.; Gao, P.; Wang, C.; Deng, F., Probing the surface of  $\gamma\text{-Al}_2\text{O}_3$  by oxygen-17 dynamic nuclear polarization enhanced solid-state NMR spectroscopy. *Phys. Chem. Chem. Phys.* **2018**, *20* (25), 17218–17225.
33. Perras, F. A.; Boteju, K. C.; Slowing, I.; Sadow, A. D.; Pruski, M., Direct  $^{17}\text{O}$  dynamic nuclear polarization of single-site heterogeneous catalysts. *Chem. Commun.* **2018**, *54* (28), 3472–3475.
34. Chen, J.; Hope, M. A.; Lin, Z.; Wang, M.; Liu, T.; Halat, D. M.; Wen, Y.; Chen, T.; Ke, X.; Magusin, P. C. M. M., et al., Interactions of Oxide Surfaces with Water Revealed with Solid-State NMR Spectroscopy. *J. Am. Chem. Soc.* **2020**, *142* (25), 11173–11182.
35. Perras, F. A.; Chaudhary, U.; Slowing, I. I.; Pruski, M., Probing Surface Hydrogen Bonding and Dynamics by Natural Abundance, Multidimensional,  $^{17}\text{O}$  DNP-NMR Spectroscopy. *J. Phys. Chem. C* **2016**, *120* (21), 11535–11544.
36. Perras, F. A.; Wang, Z.; Naik, P.; Slowing, I.; Pruski, M., Natural Abundance  $^{17}\text{O}$  DNP NMR Provides Precise O-H Distances and Insights into the Bronsted Acidity of Heterogeneous Catalysts. *Angew. Chem. Int. Ed. Engl.* **2017**, *56* (31), 9165–9169.
37. Hope, M. A.; Zhang, B.; Zhu, B.; Halat, D. M.; MacManus-Driscoll, J. L.; Grey, C. P., Revealing the Structure and Oxygen Transport at Interfaces in Complex Oxide Heterostructures via  $^{17}\text{O}$  NMR Spectroscopy. *Chem. Mater.* **2020**, *32* (18), 7921–7931.
38. MacManus-Driscoll, J. L., Self-Assembled Heteroepitaxial Oxide Nanocomposite Thin Film Structures: Designing Interface-Induced Functionality in Electronic Materials. *Adv. Funct. Mater.* **2010**, *20* (13), 2035–2045.
39. Misra, S.; Wang, H., Review on the growth, properties and applications of self-assembled oxide–metal vertically aligned nanocomposite thin films—current and future perspectives. *Mater. Horiz.* **2021**, *8*, 869–884.
40. Kudo, T.; Obayashi, H., Mixed Electrical Conduction in the Fluorite-Type  $\text{Ce}_{1-x}\text{Gd}_x\text{O}_{2-x/2}$ . *J. Electrochem. Soc.* **1976**, *123* (3), 415–419.
41. Shaikh, S. P. S.; Muchtar, A.; Somalu, M. R., A review on the selection of anode materials for solid-oxide fuel cells. *Renew. Sustain. Energy Rev.* **2015**, *51*, 1–8.
42. Corzilius, B.; Smith, A. A.; Barnes, A. B.; Luchinat, C.; Bertini, I.; Griffin, R. G., High-field Dynamic Nuclear Polarization with High-Spin Transition Metal Ions. *J. Am. Chem. Soc.* **2011**, *133* (15), 5648–5651.
43. Stevanato, G.; Kubicki, D. J.; Menzildjian, G.; Chauvin, A.-S.; Keller, K.; Yulikov, M.; Jeschke, G.; Mazzanti, M.; Emsley, L., A Factor Two Improvement in High-Field Dynamic Nuclear Polarization from Gd(III) Complexes by Design. *J. Am. Chem. Soc.* **2019**, *141* (22), 8746–8751.
44. Kaushik, M.; Bahrenberg, T.; Can, T. V.; Caporini, M. A.; Silvers, R.; Heiliger, J.; Smith, A. A.; Schwalbe, H.; Griffin, R. G.; Corzilius, B., Gd(III) and Mn(II) complexes for dynamic nuclear polarization: small molecular chelate polarizing agents and applications with site-directed spin labeling of proteins. *Phys. Chem. Chem. Phys.* **2016**, *18* (39), 27205–27218.
45. Thurber, K. R.; Tycko, R., Measurement of sample temperatures under magic-angle spinning from the chemical shift and spin-lattice relaxation rate of  $^{79}\text{Br}$  in KBr powder. *J. Magn. Reson.* **2009**, *196* (1), 84–87.
46. Bielecki, A.; Burum, D. P., Temperature Dependence of 207 Pb MAS Spectra of Solid Lead Nitrate. An Accurate, Sensitive Thermometer for Variable-Temperature MAS. *J. Magn. Reson., Ser. A* **1995**, *116* (2), 215–220.
47. Massiot, D.; Fayon, F.; Capron, M.; King, I.; Le Calvé, S.; Alonso, B.; Durand, J.-O.; Bujoli, B.; Gan, Z.; Hoatson, G., Modelling one- and two-dimensional solid-state NMR spectra. *Magn. Reson. Chem.* **2002**, *40* (1), 70–76.
48. Stoll, S.; Schweiger, A., EasySpin, a comprehensive software package for spectral simulation and analysis in EPR. *J. Magn. Reson.* **2006**, *178* (1), 42–55.
49. Pell, A. J.; Pintacuda, G.; Grey, C. P., Paramagnetic NMR in solution and the solid state. *Prog. Nucl. Magn. Reson. Spectrosc.* **2019**, *111*, 1–271.
50. Bloembergen, N.; Pound, R. V., Radiation Damping in Magnetic Resonance Experiments. *Phys. Rev.* **1954**, *95* (1), 8–12.
51. Krishnan, V. V.; Murali, N., Radiation Damping in Modern NMR Experiments: Progress and Challenges. *Prog. Nucl. Magn. Reson. Spectrosc.* **2013**, *68*, 41–57.
52. Abragam, A.; Bleaney, B., *Electron Paramagnetic Resonance of Transition Ions*. OUP Oxford: Oxford, 2012; p 147.
53. Abraham, M. M.; Boatner, L. A.; Finch, C. B.; Lee, E. J.; Weeks, R. A., Paramagnetic resonance of  $\text{Gd}^{3+}$  in  $\text{CeO}_2$  single crystals. *J. Phys. Chem. Solids* **1967**, *28* (1), 81–92.
54. de Biasi, R. S.; Grillo, M. L. N., Measurement of Small Concentrations of Gadolinium in Ceria ( $\text{CeO}_2$ ) and Magnesia ( $\text{MgO}$ ) Using Electron Magnetic Resonance. *J. Am. Ceram. Soc.* **2008**, *91* (10), 3469–3471.
55. Thurber, K. R.; Yau, W.-M.; Tycko, R., Low-temperature dynamic nuclear polarization at 9.4T with a 30mW microwave source. *J. Magn. Reson.* **2010**, *204* (2), 303–313.
56. Rossini, A. J.; Zagdoun, A.; Lelli, M.; Gajan, D.; Rascón, F.; Rosay, M.; Maas, W. E.; Copéret, C.; Lesage, A.; Emsley, L., One hundred fold overall sensitivity enhancements for Silicon-29 NMR spectroscopy of surfaces by dynamic nuclear polarization with CPMG acquisition. *Chem. Sci.* **2012**, *3* (1), 108–115.
57. Mentink-Vigier, F.; Paul, S.; Lee, D.; Feintuch, A.; Hediger, S.; Vega, S.; De Paëpe, G., Nuclear depolarization and absolute sensitivity in magic-angle spinning cross effect

- dynamic nuclear polarization. *Phys. Chem. Chem. Phys.* **2015**, *17* (34), 21824–21836.
58. Takahashi, H.; Lee, D.; Dubois, L.; Bardet, M.; Hediger, S.; De Paëpe, G., Rapid Natural-Abundance 2D  $^{13}\text{C}$ - $^{13}\text{C}$  Correlation Spectroscopy Using Dynamic Nuclear Polarization Enhanced Solid-State NMR and Matrix-Free Sample Preparation. *Angew. Chem. Int. Ed.* **2012**, *51* (47), 11766–11769.
59. Bloembergen, N., On the interaction of nuclear spins in a crystalline lattice. *Physica* **1949**, *15* (3–4), 386–426.
60. Pinon, A. C.; Schlagnitweit, J.; Berruyer, P.; Rossini, A. J.; Lelli, M.; Socie, E.; Tang, M.; Pham, T.; Lesage, A.; Schantz, S., et al., Measuring Nano- to Microstructures from Relayed Dynamic Nuclear Polarization NMR. *J. Phys. Chem. C* **2017**, *121* (29), 15993–16005.
61. Prisco, N. A.; Pinon, A. C.; Emsley, L.; Chmelka, B. F., Scaling analyses for hyperpolarization transfer across a spin-diffusion barrier and into bulk solid media. *Phys. Chem. Chem. Phys.* **2021**, *23* (2), 1006–1020.
62. Tse, D.; Hartmann, S. R., Nuclear Spin-Lattice Relaxation Via Paramagnetic Centers Without Spin Diffusion. *Phys. Rev. Lett.* **1968**, *21* (8), 511–514.
63. Ernst, M.; Meier, B., Spin diffusion in solids. 1998; pp 83–121.
64. Chang, C. A.; Francesconi, L. C.; Malley, M. F.; Kumar, K.; Gougoutas, J. Z.; Tweedle, M. F.; Lee, D. W.; Wilson, L. J., Synthesis, characterization, and crystal structures of  $\text{M}(\text{DO3A})$  ( $\text{M}$  = iron, gadolinium) and  $\text{Na}[\text{M}(\text{DOTA})]$  ( $\text{M}$  = Fe, yttrium, Gd). *Inorg. Chem.* **1993**, *32* (16), 3501–3508.
65. Becerra, L. R.; Gerfen, G. J.; Temkin, R. J.; Singel, D. J.; Griffin, R. G., Dynamic nuclear polarization with a cyclotron resonance maser at 5 T. *Phys. Rev. Lett.* **1993**, *71* (21), 3561–3564.
66. Lelli, M.; Chaudhari, S. R.; Gajan, D.; Casano, G.; Rossini, A. J.; Ouari, O.; Tordo, P.; Lesage, A.; Emsley, L., Solid-State Dynamic Nuclear Polarization at 9.4 and 18.8 T from 100 K to Room Temperature. *J. Am. Chem. Soc.* **2015**, *137* (46), 14558–14561.
67. Inaba, H.; Tagawa, H., Ceria-based solid electrolytes - Review. *Solid State Ionics* **1996**, *83* (1-2), 1–16.
68. Grieshammer, S.; Grope, B. O.; Koettgen, J.; Martin, M., A combined DFT + U and Monte Carlo study on rare earth doped ceria. *Phys. Chem. Chem. Phys.* **2014**, *16* (21), 9974–86.
69. Yang, S. M.; Lee, S.; Jian, J.; Zhang, W.; Lu, P.; Jia, Q.; Wang, H.; Noh, T. W.; Kalinin, S. V.; MacManus-Driscoll, J. L., Strongly enhanced oxygen ion transport through samarium-doped  $\text{CeO}_2$  nanopillars in nanocomposite films. *Nat. Commun.* **2015**, *6*, 8588.
70. Zhu, B.; Schusteritsch, G.; Lu, P.; MacManus-Driscoll, J. L.; Pickard, C. J., Determining interface structures in vertically aligned nanocomposite films. *APL Materials* **2019**, *7* (6), 061105.
71. Björgvinsdóttir, S.; Moutzouri, P.; Walder, B. J.; Matthey, N.; Emsley, L., Hyperpolarization transfer pathways in inorganic materials. *J. Magn. Reson.* **2021**, *323*, 106888.



# Supplementary Information

## Endogenous $^{17}\text{O}$ DNP of Gd-Doped $\text{CeO}_2$ from 100 to 370 K

Michael A. Hope,<sup>1,2</sup> Snædís Björgvinsdóttir,<sup>1</sup> David M. Halat,<sup>2</sup> Georges Menzildjian,<sup>3</sup> Zhuoran Wang,<sup>3</sup> Bowen Zhang,<sup>4</sup> Judith L. MacManus-Driscoll,<sup>4</sup> Anne Lesage,<sup>3</sup> Moreno Lelli,<sup>5,6</sup> Lyndon Emsley,<sup>1,\*</sup> Clare P. Grey<sup>2,\*</sup>

1. *Institut des Sciences et Ingénierie Chimiques, Ecole Polytechnique Fédérale de Lausanne (EPFL), CH-1015 Lausanne, Switzerland*
2. *Department of Chemistry, University of Cambridge, Lensfield Road, Cambridge, CB2 1EW, UK.*
3. *Centre de RMN à Très Hauts Champs, Université de Lyon (CNRS/ENS de Lyon/UCB-Lyon 1), 69100 Villeurbanne, France.*
4. *Department of Materials Science and Metallurgy, University of Cambridge, Cambridge, CB3 0FS, UK.*
5. *Magnetic Resonance Center (CERM), Department of Chemistry "Ugo Schiff", University of Florence, 50019 Sesto Fiorentino, Italy*
6. *Consorzio Interuniversitario Risonanze Magnetiche MetalloProteine (CIRMMP), via Sacconi 6, 50019 Sesto Fiorentino, Italy*

Raw and processed NMR and EPR data are available at DOI: [10.5281/zenodo.5101215](https://doi.org/10.5281/zenodo.5101215).

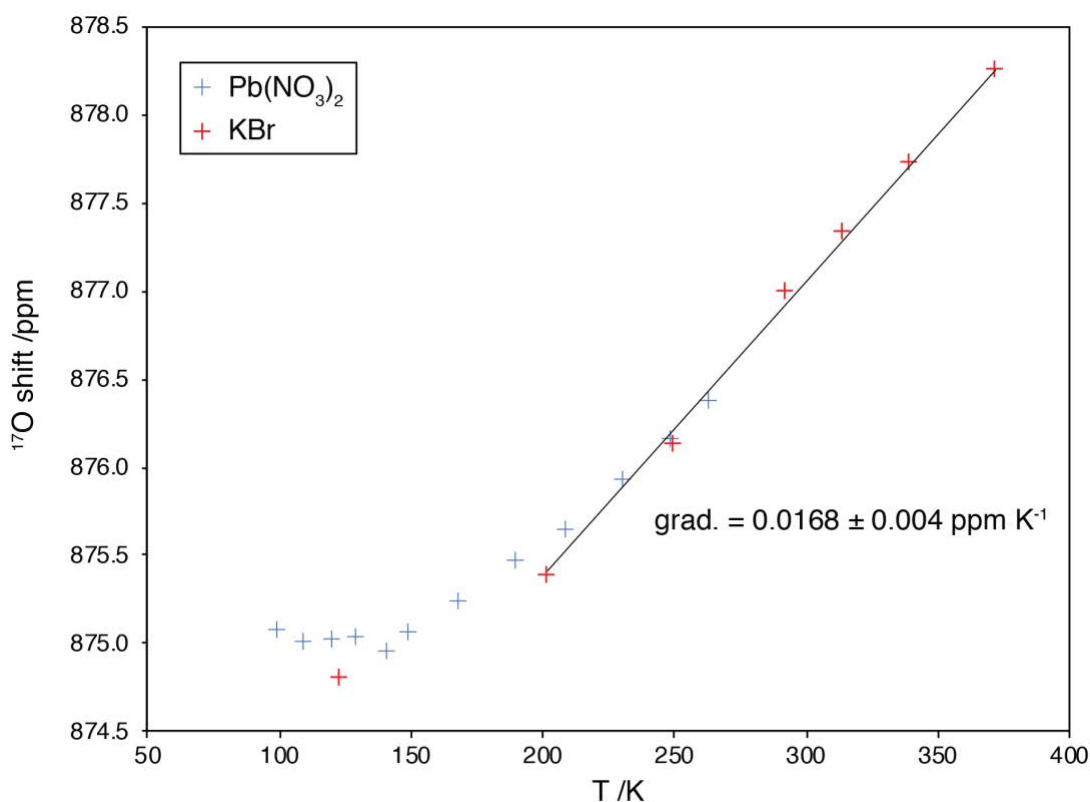


Figure S1:  $^{17}\text{O}$  shift as a function of temperature for  $^{17}\text{O}$ -enriched 0.01% Gd- $\text{CeO}_2$ . In two sets of experiments the temperature was measured from the  $^{79}\text{Br}$   $T_1$  of KBr and the  $^{207}\text{Pb}$  shift of  $\text{Pb}(\text{NO}_3)_2$ , respectively. In the former, the  $^{79}\text{Br}$  shift was also used to account for any field drift, once its temperature dependence had also been included.

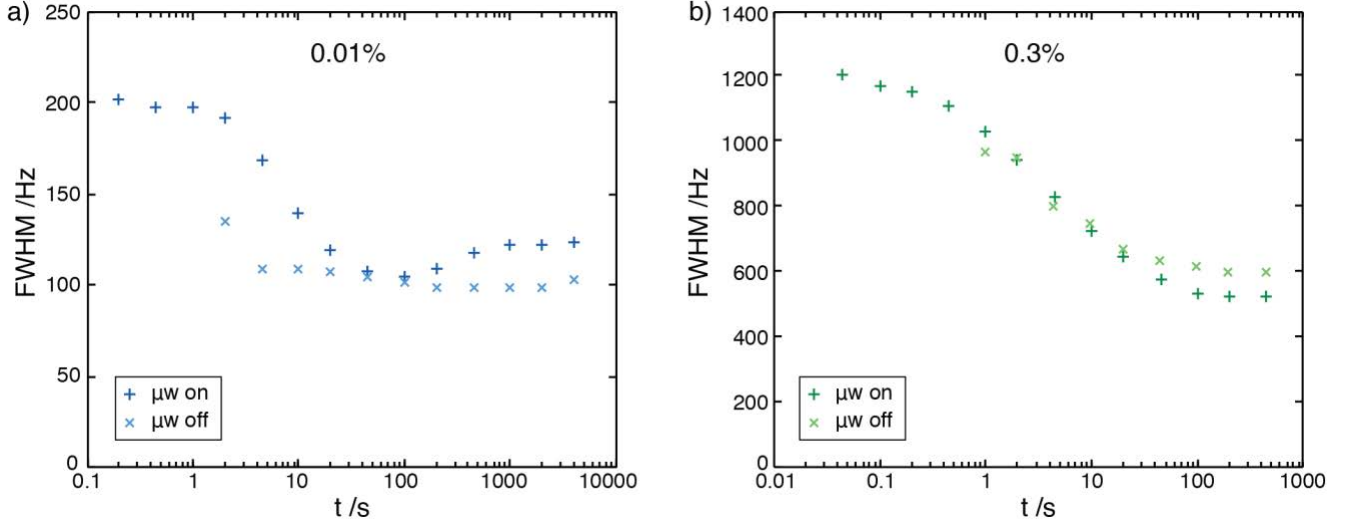


Figure S2: Full-width-at-half-maximum (FWHM) of the  $^{17}\text{O}$  NMR signal in  $^{17}\text{O}$  enriched a) 0.01% and b) 0.3% Gd- $\text{CeO}_2$  as a function of buildup time with and without microwave irradiation. In both cases the line is broader at shorter buildup times because nuclei closer to  $\text{Gd}^{3+}$ , experiencing greater broadening, build up faster. However, whereas the linewidth for 0.3% Gd- $\text{CeO}_2$  decreases monotonically in line with  $T_{\text{DNP}}$ , the linewidth for 0.01% Gd- $\text{CeO}_2$  increases again at longer buildup times due to radiation damping. Radiation damping depends on the size of the magnetization, and therefore follows the same buildup as the magnetization, only becoming significant above 100 s (c.f. Figure S7). Note that the scales in a) and b) are not the same. It was not possible to accurately measure the linewidth without microwave irradiation at short build-up times due to poor signal-to-noise.

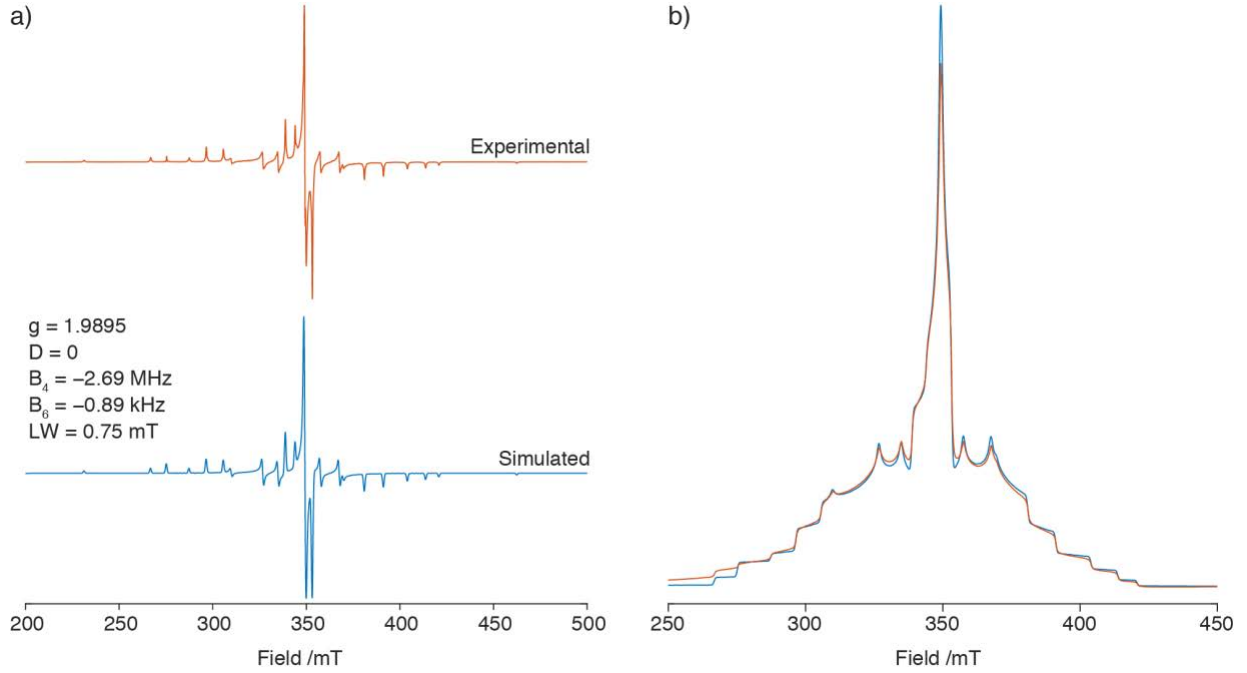


Figure S3: a) Derivative and b) integrated X-band EPR spectra of 0.01% Gd- $\text{CeO}_2$  with  $\nu_0 = 9.6226$  GHz and simulated spectra with the given parameters. LW is the gaussian linewidth, D is the 2<sup>nd</sup>-rank ZFS, and  $B_4$  and  $B_6$  are the 4<sup>th</sup> and 6<sup>th</sup> rank ZFS constants, respectively, giving rise to the following terms in the Hamiltonian:  $B_4(\hat{O}_4^0 + 5\hat{O}_4^4)$  and  $B_6(\hat{O}_6^0 - 21\hat{O}_6^4)$ , where  $\hat{O}_k^q$  are the Stevens operators for crystal field splitting.

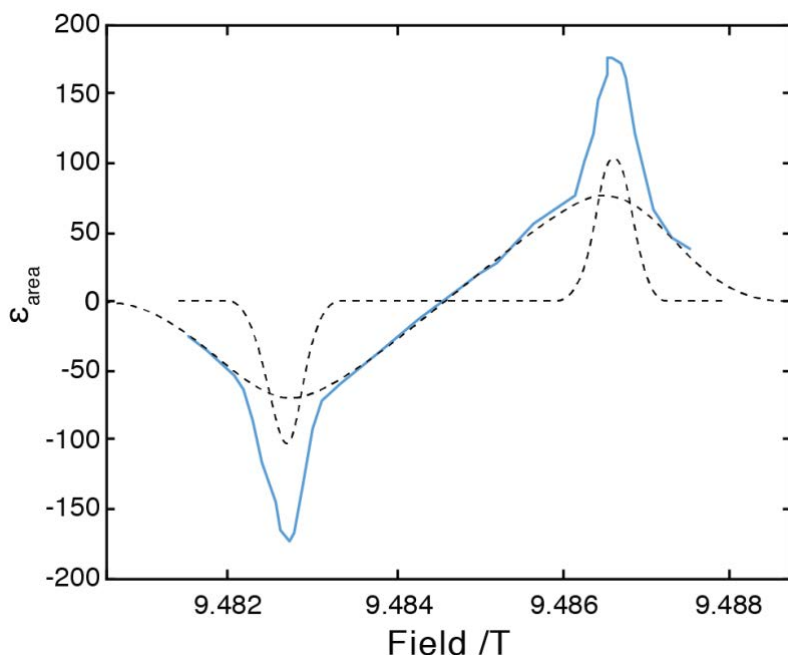


Figure S4: Schematic deconvolution of the sharp and broad components in the DNP field profile of  $^{17}\text{O}$ -enriched 0.01% Gd-CeO<sub>2</sub>, recorded with a 10 s recycle delay and a 265 GHz klystron microwave source.

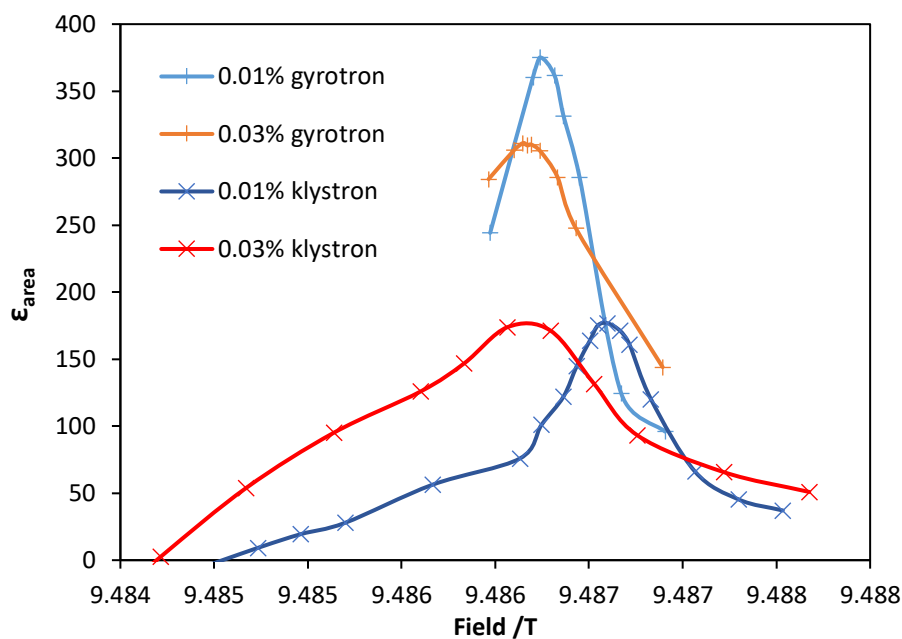


Figure S5: Comparison of the  $^{17}\text{O}$  DNP field profiles recorded for 0.01% and 0.03% Gd-CeO<sub>2</sub> recorded with klystron and gyrotron microwave sources, using a 10 second recycle delay. The gyrotron data has been offset by 26.7 mT to align the maxima of the 0.03% sample. The offset between the maxima of the two samples is far smaller when the gyrotron was used than when the klystron was used, therefore in the latter case the offset is ascribed to slight variations (<30 ppm) in the microwave frequency. The slight remaining offset between the maxima for the two samples most likely arises from the different relative contributions of the sharp and broad components of the enhancement profiles.

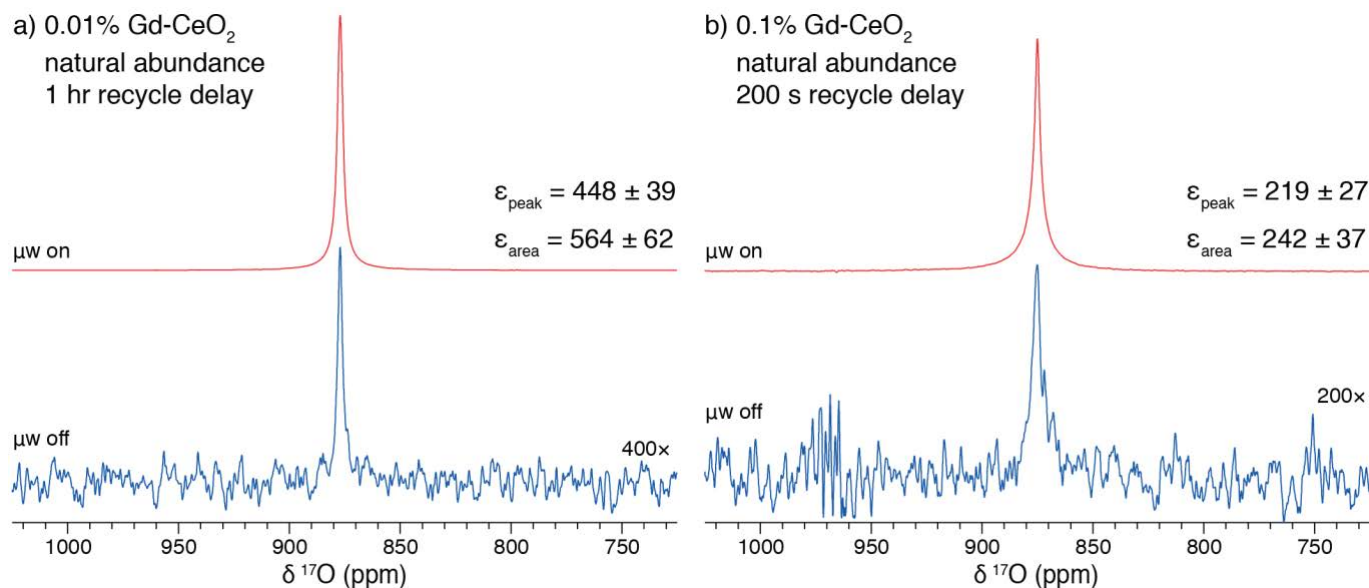


Figure S6:  $^{17}\text{O}$  spectra of natural abundance a) 0.01% and b) 0.1% Gd- $\text{CeO}_2$ , with and without microwave irradiation. The microwave on spectra were recorded with four scans, while the microwave off spectra required 8 and 32 scans for (a) and (b), respectively.

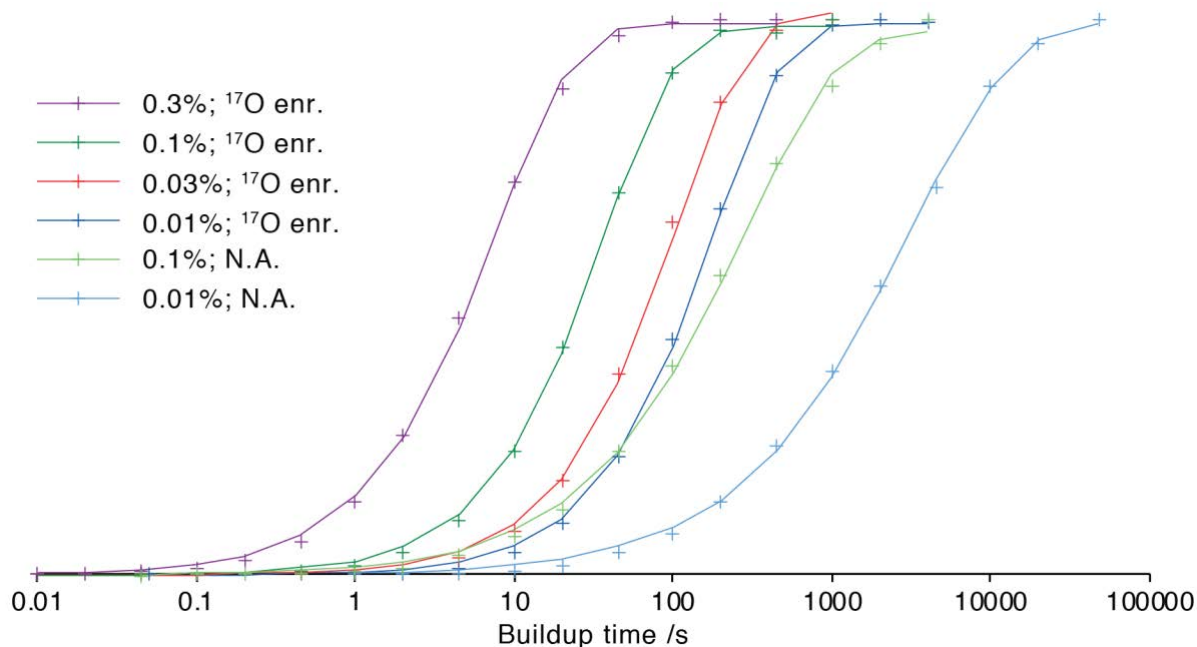


Figure S7:  $^{17}\text{O}$  DNP buildup curves measured using a saturation recovery experiment for Gd- $\text{CeO}_2$  with different concentrations of Gd, 0.01% – 0.3%, both with  $^{17}\text{O}$  enrichment and at natural abundance. The crosses are experimental data points and the solid lines are fits to a stretched exponential function,  $I = I_0 \left( 1 - \exp \left[ - \left( \frac{t}{T_B} \right)^\beta \right] \right)$  with the parameters shown in Table 1.

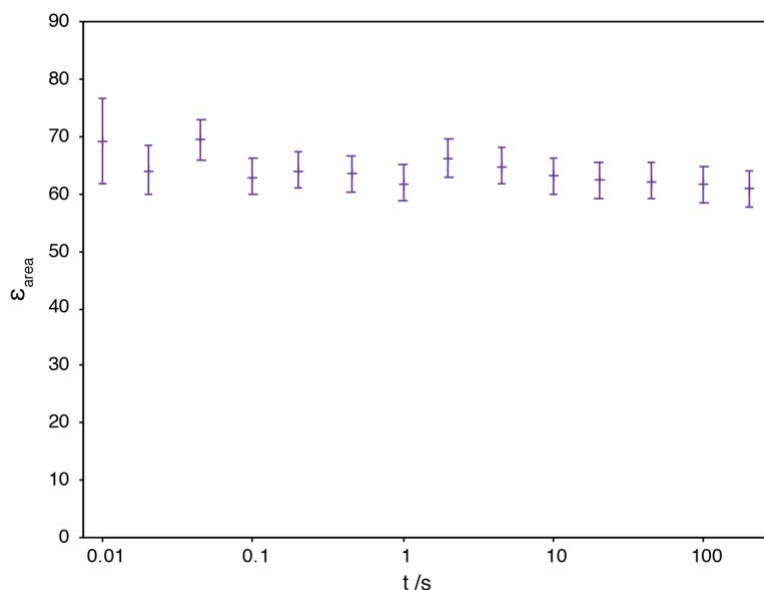


Figure S8:  $^{17}\text{O}$  enhancement factor by area as a function of buildup time for  $^{17}\text{O}$ -enriched 0.3% Gd-CeO<sub>2</sub>, recorded at 10 kHz MAS and 100 K. A zirconia rotor was used resulting in slightly lower enhancements than with a sapphire rotor, as in the main text.

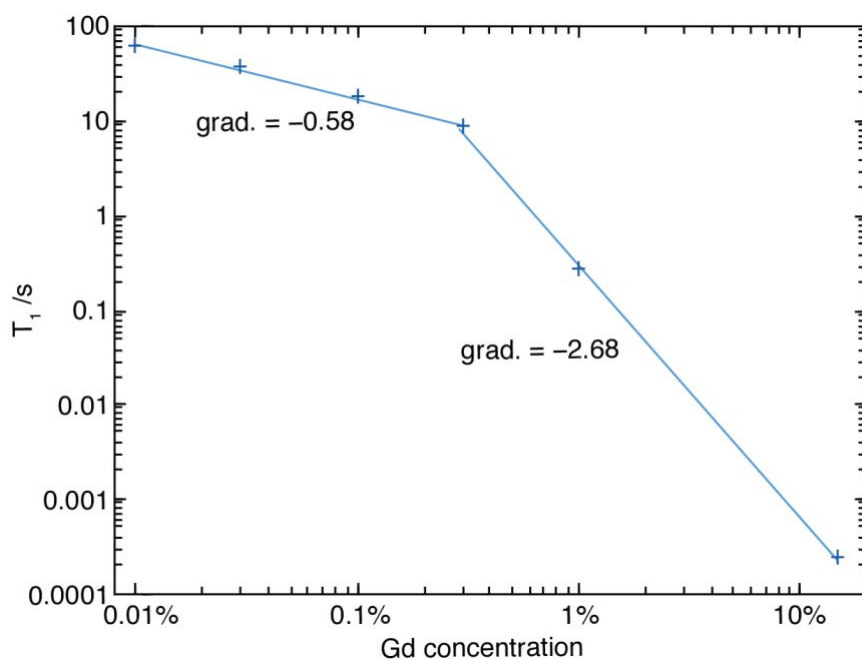


Figure S9: Log-log plot of  $^{17}\text{O}$   $T_1$  at room temperature as a function of Gd concentration in  $^{17}\text{O}$ -enriched Gd-CeO<sub>2</sub>, showing a change of gradient at a concentration of 0.3%. When relaxation occurs by spin diffusion from paramagnetic centres,  $1/T_1 \propto c_{\text{Gd}}$ , whereas when the nuclei relax directly  $1/T_1 \propto c_{\text{Gd}}^2$ . The discrepancy between the expected exponents (i.e.  $-1$  and  $-2$ , respectively) and the observed exponents ( $-0.58$  and  $-2.68$ , respectively) may be due to a concentration dependence of the Gd<sup>3+</sup> electronic relaxation, due to electron–electron interactions, which in turn affects the efficiency of nuclear relaxation.

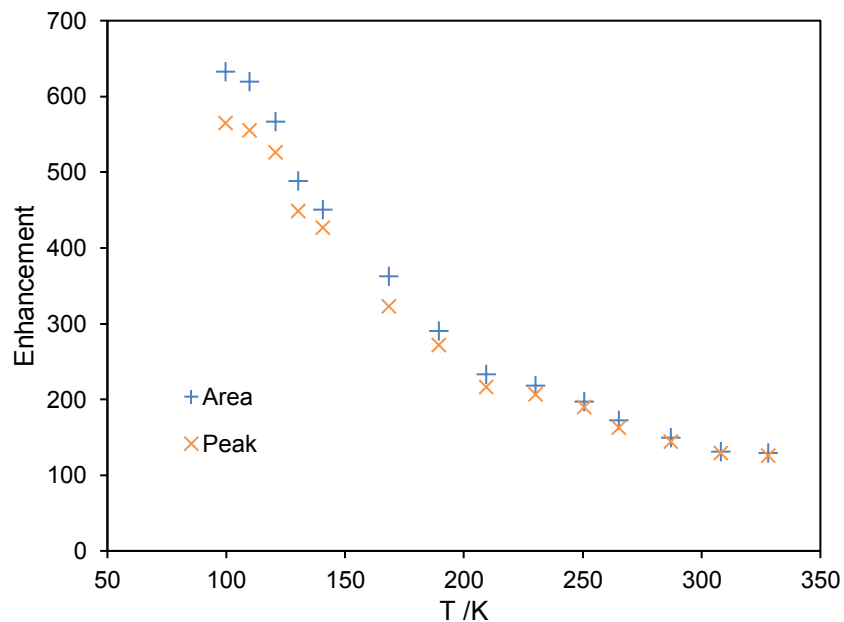


Figure S10:  $^{17}\text{O}$  DNP enhancement by peak intensity and by area as a function of temperature for  $^{17}\text{O}$ -enriched 0.01% Gd-doped  $\text{CeO}_2$  with  $\sim 14$  W of microwave irradiation at 10 kHz MAS. The line-broadening due to radiation damping decreases with increasing temperature due to the reduction in nuclear spin polarisation, therefore the difference between the linewidths with and without microwave irradiation decreases, and the peak and areal enhancements become similar.

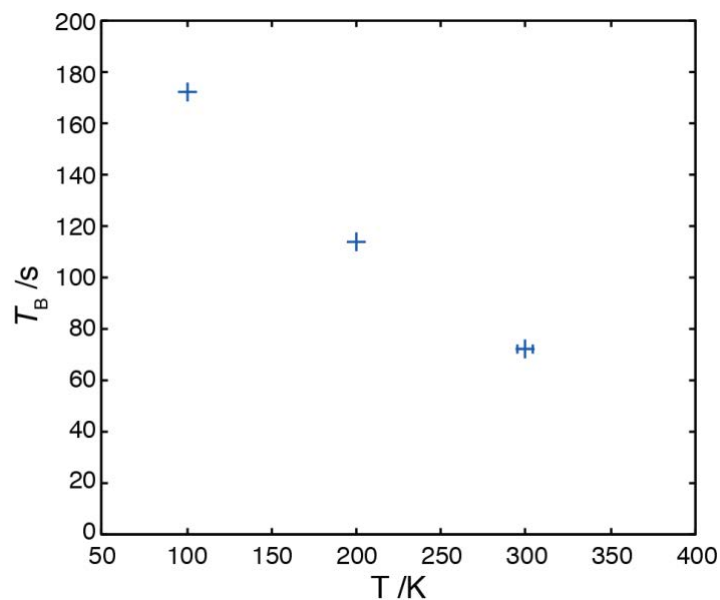


Figure S11: Buildup time constant,  $T_B$ , for  $^{17}\text{O}$  DNP of  $^{17}\text{O}$ -enriched 0.01% Gd- $\text{CeO}_2$  as a function of temperature at 10 kHz MAS with  $\sim 14$  W of microwave irradiation.



Table S1: Sensitivity factor (final column) as a function of temperature, as determined by the enhancement, sample temperature, and build-up time constant, for  $^{17}\text{O}$  DNP of 0.01% Gd-CeO<sub>2</sub>.

T /K	$\varepsilon_{\text{area}}$ (interpolated)	$T_{\text{DNP}} / \text{s}$	$\frac{\varepsilon_{\text{area}}}{T\sqrt{T_{\text{DNP}}}} / \text{K}^{-1}\text{s}^{-0.5}$
100	632	172	0.482
200	262	113.6	0.123
300	140	72.52	0.055

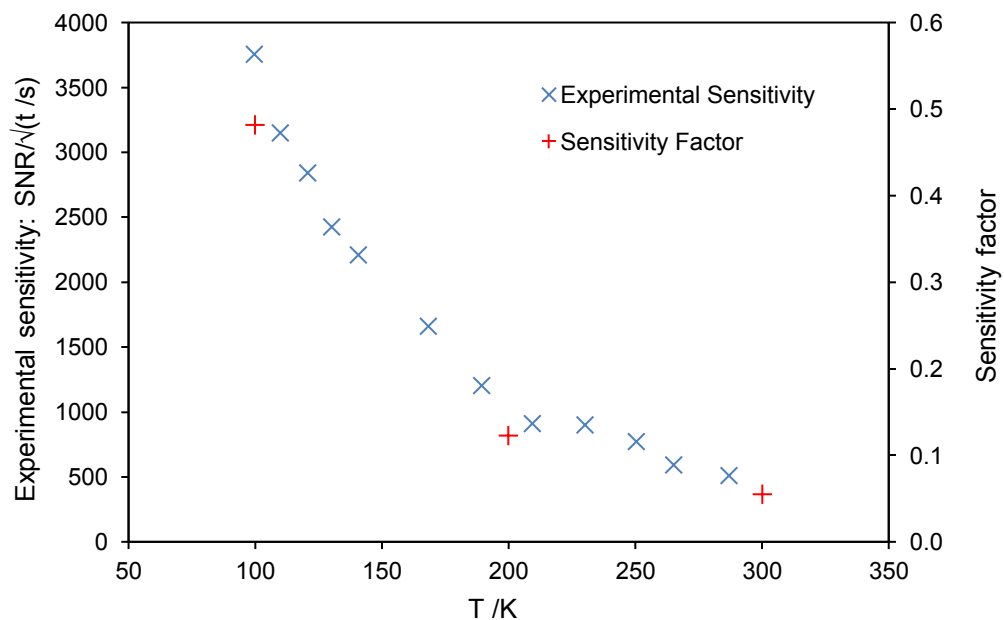


Figure S12: The experimental sensitivity, given by the signal-to-noise ratio per square-root time, and the sensitivity factor calculated in Table S1 for  $^{17}\text{O}$  DNP of 0.01% Gd-CeO<sub>2</sub> as a function of temperature.

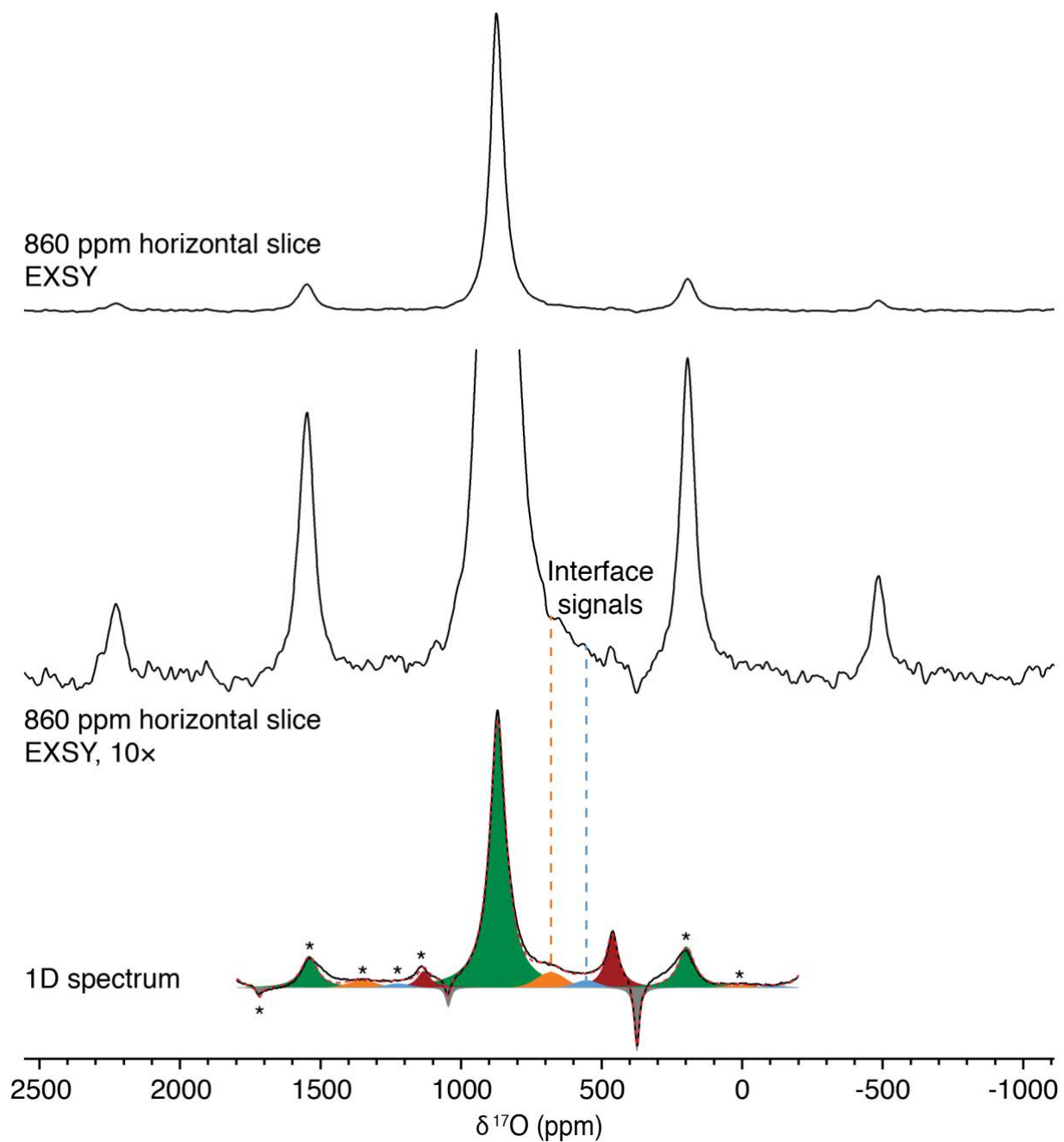


Figure S13: Horizontal slice at 860 ppm from the 2D DNP-enhanced  $^{17}\text{O}$  EXSY spectrum of 1% Gd-doped  $\text{CeO}_2\text{-SrTiO}_3$  VAN films (Figure 6b) compared with the 1D DNP-enhanced spectrum (Figure 6a), showing weak signal intensity corresponding to cross peaks with the interface environments at 685 ppm and 465 ppm.

Table S2: Experimental parameters and enhancements for different  $^{17}\text{O}$  spectra shown in this work.

Sample	Figure/Table	MAS /kHz	Recycle delay /s	Approx. $\mu\text{W}$ power /W	$\epsilon_{\text{area}}$
0.01% Gd $^{17}\text{O}$ enr.	Figure 1 Table 1	10	200	14	652(5)
	Figure 3a	10	100	14	632(5)
0.03% Gd $^{17}\text{O}$ enr.	Figure 3a Table 1	10	100	22	389(4)
0.1% Gd $^{17}\text{O}$ enr.	Figure 3a Table 1	10	100	22	162(3)
0.3% Gd $^{17}\text{O}$ enr.	Figure 3a	10	100	34	78(2)
	Table 1	10	10	34	81(2)
1% Gd $^{17}\text{O}$ enr.	Figure 3a	10	100	41	8.8(2)
0.01% Gd Nat. abund.	Table 1	10	20,000	14	611(92)
	Figure S6	10	3600	14	564(62)
0.1% Gd Nat. abund.	Table 1	10	200	14	242(37)
	Figure S6	10	200	14	242(37)
0.3% Gd Nat. abund.	Table 1	10	100	30	112(7)

### Supplementary Note 1:

A note on the scaling of spin diffusivity with concentration.<sup>63</sup> In a cubic crystal, the spin diffusion constant depends on the probability of a flip–flop transition,  $W$ , and the separation of the spins,  $r$  as

$$D = Wr^2.$$

$W$  is proportional to the square of the dipolar coupling strength,  $d$ , which in turn depends on  $r^{-3}$ :

$$W \propto d^2 \propto 1/r^6.$$

Therefore, in the absence of any other dependence on  $r$ , the spin diffusivity scales as:

$$D \propto 1/r^4 \propto c^{4/3},$$

where  $c \propto 1/r^3$  is the concentration of the spins. However,  $W$  is also inversely proportional to the zero-quantum linewidth, and therefore proportional to the zero-quantum  $T_2$ :

$$W \propto d^2 T_2^{\text{ZQ}}.$$

For abundant, high- $\gamma$  nuclei like protons, the zero-quantum linewidth is determined by homonuclear dipolar coupling and therefore also depends on the dipolar coupling constant,  $T_2^{\text{ZQ}} \propto 1/d$ . This changes the scaling of  $W$  and therefore  $D$ :

$$W \propto d^2 T_2^{\text{ZQ}} \propto d \propto 1/r^3$$

$$D \propto Wr^2 \propto 1/r \propto c^{1/3}.$$

Therefore for nuclei where the zero-quantum lineshape is dominated by homonuclear dipolar coupling we have  $D \propto c^{1/3}$ , whereas for lower- $\gamma$  and/or lower abundance nuclei we have  $D \propto c^{4/3}$ , as is the case for  $^{17}\text{O}$ .